



Norwegian University of  
Science and Technology

# Wake behind a horizontal-axis wind turbine

Øyvind Vik Nygard

Master of Science in Energy and Environment

Submission date: June 2011

Supervisor: Per-Åge Krogstad, EPT



EPT-M-2011- 75

**MASTER THESIS**

for

**Stud.techn. Øyvind Vik Nygard**

Spring 2011

Wake behind a horizontal -axis wind turbine

*Vake bak tårnet til en horisontalakslet vindturbin***Background and objective**

Behind every object in a flow there will be a wake where the flow speed is reduced compared to the inflow speed. This is also the case for a wind turbine, where both the rotor and tower will generate wakes. Most wind turbine towers are cylindrical due to rotation symmetry. For cylinders there are classical solutions for how the wake develops in the flow direction. However for wind turbines these classical solutions cannot be used because of the strong interaction between the wake from the rotor and the one generated by the tower. This influence starts as soon as the flow leaves the tower. Since the wake from the rotor largely generates vortices normal to the tower, it is reason to believe that the wake behind the tower will die out faster than behind a free-standing cylinder. It is desirable to study the development of the wake and see how it is affected by the operating conditions of the wind turbine.

The student should consider the following questions:

- Learn how to use measuring equipment to study turbulent flow and use it on a simple free-standing cylinder. This will form the benchmark for the turbine wake and at the same time give an indication of the expected accuracy.
- Map the wake in the area behind the tower as a function of the streamwise distance from the tower when the turbine operates at its design condition.
- Repeat the measurements when the wind turbine operates a lower and higher tip speed ratios. The tip speed ratios should be chosen so that the power output is about half of the output at best point operation.
- Discuss the results and compare measurements and classical theory for the wake behind a free-standing cylinder.

Within 14 days of receiving the written text on the master thesis, the candidate shall submit a research plan for his project to the department.

When the thesis is evaluated, emphasis is put on processing of the results, and that they are presented in tabular and/or graphic form in a clear manner, and that they are analyzed carefully.

The thesis should be formulated as a research report with summary both in English and Norwegian, conclusion, literature references, table of contents etc. During the preparation of the text, the candidate should make an effort to produce a well-structured and easily readable report. In order to ease the evaluation of the thesis, it is important that the cross-references are correct. In the making of the report, strong emphasis should be placed on both a thorough discussion of the results and an orderly presentation.

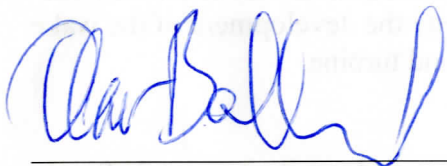
The candidate is requested to initiate and keep close contact with his/her academic supervisor(s) throughout the working period. The candidate must follow the rules and regulations of NTNU as well as passive directions given by the Department of Energy and Process Engineering.

Pursuant to "Regulations concerning the supplementary provisions to the technology study program/Master of Science" at NTNU §20, the Department reserves the permission to utilize all the results and data for teaching and research purposes as well as in future publications.

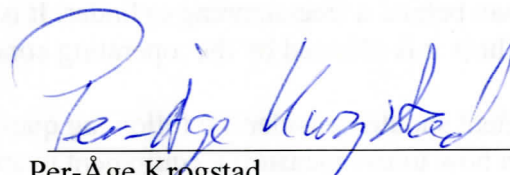
One – 1 complete original of the thesis shall be submitted to the authority that handed out the set subject. (A short summary including the author's name and the title of the thesis should also be submitted, for use as reference in journals (max. 1 page with double spacing)).

Two – 2 – copies of the thesis shall be submitted to the Department. Upon request, additional copies shall be submitted directly to research advisors/companies. A CD-ROM (Word format or corresponding) containing the thesis, and including the short summary, must also be submitted to the Department of Energy and Process Engineering

Department of Energy and Process Engineering, 10. January 2011



Olav Bolland  
Department Head



Per-Åge Krogstad  
Academic Supervisor

Research Advisors:



## **Preface**

This master thesis has been carried out at the Department of Energy and Process Engineering at The Norwegian University of Science and Technology in the spring of 2011. The work has been done over a period of 20 weeks and counts for 30 credit points.

There have been a lot more laboratory work than expected, and even though it has been frustrating along the way, it is very rewarding when things work out and good results are obtained. With such an enormous amount of experimental data gathered, a lot of time has been used on post-processing of data to present the results in the most compact and understandable way.

I would like to thank my advisor Professor Per-Åge Krogstad for help and guidance through the process, Arnt Egil Kolstad for helping out in the workshop, Pål Egil Eriksen for sharing his knowledge on wind tunnel experimenting, Fabio Pirrela for the super-version on Genlog and my co-students and friends for helpful discussions and motivation along the way. I would also like to thank my girlfriend Kari Sørnes for supporting and bearing with me when I was spending the better part of the day (and night) in the laboratory.



Øyvind Vik Nygard, NTNU , June 2011.

## Abstract

In this paper theory on cylinder and wind turbine wakes have been studied, and experimental work on the wake behind a wind turbine have been carried out in the Fluids engineering laboratory at NTNU.

The objective of this paper is to show and explain how the wake from the tower of a wind turbine develops and interacts with the rotor wake. It is desirable to study the wake for different operating conditions of the wind turbine to see how the wake development is affected. A summary of classical wake theory, aerodynamics and wind turbine wakes will be given. Measurements in the wake of a cylinder fitted with pressure taps for drag calculation will be compared to theory and used as a reference. Also, the wake behind the wind turbine tower with the blades taken off will be studied and compared to the tower wake found behind the operating wind turbine.

For comparison, reference measurements were done in the wake behind a cylinder and behind the free standing wind turbine tower without blades. The drag coefficient obtained from pressure measurements on the cylinder surface were 1.077 and match the expected value of 1.2 fairly well. However, neither the shape nor the maximum velocity deficit measured in the wake fit the theoretical profile. Drag coefficients calculated from the momentum deficit across the wake were only in the range of 0.65, which is almost half of the expected, and the huge deviation from theory could not be explained. With values between 1.07 and 1.50 the measured drag coefficients in the wake of the tower alone were also not consistent with theory. The shape of the tower wake profile coincides better with theory than the cylinder wake, but the maximum velocity deficit is generally lower than predicted by theory. Difference in drag can be explained with blockage effect and the smaller velocity deficit may be attributed to the free stream flow over the top of the tower interfering with the wake downstream of the tower.

Wake surveys behind the wind turbine were done at three operating conditions: Optimum tip speed ratio; low tip speed ratio, with power output half of output at best point operation; and high tip speed ratio, with power output half of output at best point operation.

The increased turbulence level behind the rotor the flow seen by the tower is believed to creates a turbulent boundary layer which stays attached to the surface to a point further back on the tower, creating a narrower and weaker wake compared the free standing tower wake. Optimum turbine operation gives a stronger rotation of the wake due to the higher torque on the blades compared to the two other cases. At high TSR the wake is more uniform, and the tower wake disappears faster than in the wake of the turbine operating at lower TSR. The Strouhal number found in all the wakes match well with theory and does not seem to be affected by the rotor wake except that the tower vortices dies out quicker.

# Contents

- 1 Introduction** **1**
  
- 2 Theory** **2**
  - 2.1 The atmosphere . . . . . 2
    - 2.1.1 The atmospheric boundary layer . . . . . 2
      - 2.1.1.1 Stability . . . . . 2
    - 2.1.2 Wind speed variation with height . . . . . 4
      - 2.1.2.1 Roughness length . . . . . 4
      - 2.1.2.2 Logarithmic profile . . . . . 5
      - 2.1.2.3 Power-law profile . . . . . 5
    - 2.1.3 Turbulence . . . . . 6
  - 2.2 Flow around a cylinder . . . . . 7
    - 2.2.1 Potential flow . . . . . 8
      - 2.2.1.1 The stream function . . . . . 8
      - 2.2.1.2 Elementary flows . . . . . 9
    - 2.2.2 Viscous flow around a cylinder . . . . . 11
    - 2.2.3 Wake theory . . . . . 12
    - 2.2.4 Drag and drag coefficient . . . . . 16
      - 2.2.4.1  $C_d$  from velocity deflection in wake . . . . . 17
      - 2.2.4.2  $C_d$  from pressure distribution on cylinder . . . . . 17
  - 2.3 Wind turbine aerodynamics . . . . . 19
    - 2.3.1 Theoretical power production . . . . . 19
      - 2.3.1.1 Aerodynamics of the airfoil . . . . . 23
    - 2.3.2 Wind Turbine Wakes . . . . . 24
      - 2.3.2.1 Wake rotation . . . . . 24
      - 2.3.2.2 Turbulence intensity . . . . . 25
      - 2.3.2.3 Expected tower influence . . . . . 25
  
- 3 Experimental set-up** **26**
  - 3.1 Instruments and facilities . . . . . 26
    - 3.1.1 Calibration . . . . . 26
      - 3.1.1.1 Pitot . . . . . 26
      - 3.1.1.2 Thrust and torque . . . . . 27
      - 3.1.1.3 Hot wire . . . . . 28
  - 3.2 Reference experiment - wake behind a cylinder . . . . . 29

3.3	Main experiment- wake behind a wind turbine . . . . .	30
3.3.1	Tower wake . . . . .	30
3.3.2	Turbine operation . . . . .	30
3.3.3	Grid size . . . . .	31
3.3.4	Wind speed . . . . .	31
3.3.5	Blockage and scaling effects . . . . .	32
3.3.6	Similarity criteria . . . . .	33
<b>4</b>	<b>Results</b>	<b>35</b>
4.1	Reference experiment behind cylinder in small wind tunnel . . . . .	35
4.2	Large wind tunnel . . . . .	38
4.2.1	$C_P$ and $C_T$ . . . . .	38
4.2.2	Tower wake . . . . .	38
4.2.3	Wind turbine wake . . . . .	42
4.2.4	Comparison of wake profiles . . . . .	44
4.2.4.1	Wake of turbine operating at optimum TSR . . . . .	46
4.2.4.2	Wake of turbine operating at low TSR . . . . .	47
4.2.4.3	Wake of turbine operating at high TSR . . . . .	48
4.2.4.4	PSD in wind turbine wake . . . . .	49
<b>5</b>	<b>Discussion</b>	<b>52</b>
5.1	Reference measurements behind cylinder in small wind tunnel . . . . .	52
5.2	Large wind tunnel . . . . .	53
5.2.1	$C_P$ and $C_T$ . . . . .	53
5.2.2	Tower wake . . . . .	53
5.2.3	Wind turbine wake . . . . .	55
5.2.4	Comparison of velocity deficit in the wake profiles . . . . .	55
5.2.4.1	Wake behind wind turbine operating at optimum TRS . . . . .	56
5.2.4.2	Wake behind wind turbine operating at low TSR . . . . .	56
5.2.4.3	Wake behind wind turbine operating at high TRS . . . . .	56
5.2.4.4	PSD analysis . . . . .	57
5.3	Uncertainty . . . . .	58
<b>6</b>	<b>Conclusion</b>	<b>60</b>
<b>7</b>	<b>Further work</b>	<b>61</b>

<b>Bibliography</b>	<b>62</b>
<b>A Calibration</b>	<b>64</b>
A.1 Calibration data . . . . .	64
A.2 Calibration curves . . . . .	66
<b>B Reference speed</b>	<b>67</b>
<b>C Experimental data</b>	<b>68</b>
C.1 Wake measurements . . . . .	68
C.2 Pressure measurments on cylinder surface . . . . .	69
C.3 $C_P$ and $C_T$ . . . . .	70
C.4 TI plots from $x=1.5D$ . . . . .	71



## List of Figures

1	Relation between Reynolds number and drag coefficient [26] . . . . .	8
2	Elementary flows . . . . .	10
3	Turbulent/high Reynolds number flow around a cylinder . . . . .	12
4	laminar/low Reynolds number flow around a cylinder . . . . .	12
5	Strouhal number as a function of Reynolds number behind a circular cylinder [26] . . . . .	13
6	Sketch of wake behind cylinder, showing key variables . . . . .	13
7	$C_p$ distribution on a cylinder for ideal flow (dash-dot-line), subcritical Reynolds number (dashed line) and supercritical Reynolds number (solid line) [5] . . . .	18
8	Illustration of flow through a wind turbine using 1D momentum theory . . . . .	19
9	Wind speed, angle of attack and forces on a blade element . . . . .	22
10	Stalled airfoil [13] . . . . .	23
11	$C_l$ and $C_d$ vs $\alpha$ for airfoil operating at different levels of turbulence with $Re=400,000$ [9]	24
12	Calibration of thrust and torque (modified from [6]) . . . . .	27
13	The wind tunnel set-up and cylinder used in reference experiment . . . . .	29
14	Wind tunnel set-up . . . . .	30
15	The model wind turbine . . . . .	31
16	Wind speed and TI in empty tunnel . . . . .	35
17	$C_p$ on cylinder surface . . . . .	36
18	Non-dimensional velocity profiles in the wake . . . . .	36
19	Turbulence intensity in wake . . . . .	37
20	PSD for the cylinder wake . . . . .	37
21	$C_p$ and $C_t$ curves . . . . .	38
22	Non-dimensional velocity profiles in the tower wake . . . . .	39
23	Turbulence intensities in tower wake . . . . .	40
24	Vertical velocity profiles at wake center . . . . .	40
25	Measured growth rates for $y_{\frac{1}{2}}$ and $\Delta u_{max}$ . . . . .	41
26	PSD for the tower wake . . . . .	42
27	Wake velocity profiles at $z = -0.3 R$ . . . . .	44
28	Wake velocity profiles at $z = -R$ . . . . .	45
29	Streamwise velocity in the wake of the turbine operating at $TSR=4.0$ . . . . .	46
30	Streamwise TI in the wake of the turbine operating at $TSR=4.0$ . . . . .	46
31	Streamwise velocity in the wake of the turbine operating at $TSR=3.0$ . . . . .	47
32	Streamwise TI in the wake of the turbine operating at $TSR=3.0$ . . . . .	47

33	Streamwise velocity in wake of the turbine operating at TSR=6.25 . . . . .	48
34	Streamwise TI in wake of the turbine operating at TSR=6.25 . . . . .	48
35	PSD for wind turbine wake operating at TSR=4.0 . . . . .	49
36	PSD for wind turbine wake operating at TSR=3.0 . . . . .	50
37	PSD for wind turbine wake operating at TSR=6.25 . . . . .	51
38	Data for calibration of transducers used for pitot measurements of reference and wake speed, and an example of the hw calibration . . . . .	64
39	Data from calibration of thrust and torque scales . . . . .	65
40	Calibration curves . . . . .	66
41	Ratio of speed at hub height vs speed measured at the contraction . . . . .	67
42	Exaple of data gathered in wake measurements . . . . .	68
43	Data from pressure measurements on cylinder surface . . . . .	69
44	Data from $C_P$ and $C_T$ experiments . . . . .	70
45	Contour plots of streamwise TI from $x=1.5D$ for TSR=3.0 and TSR=4.0 . . . .	71

## List of Tables

1	Terrain categories and corresponding roughness lengths in Eurocode [1] . . . .	4
2	Summary of results (exp) and theory (th) from cylinder wake measurements . .	35
3	Summary of results (exp) and theory (th) from tower wake measurements . . .	39
4	Wind turbine operating conditions . . . . .	43
5	Summary of results from wind turbine wake measurements . . . . .	43

## Nomenclature

### Roman

a	Axial induction factor
A	Area
$A_R$	Rotor area
b	Half wake width
$C_\theta$	Azimuthal component of wake velocity
$C_P$	Power coefficient
$C_T$	Thrust coefficient
$C_d$	Drag coefficient
$C_p$	Pressure coefficient
$c_p$	Specific heat capacity
d	Drag force
D	Diameter of object
$D_R$	Diameter of rotor
E	Voltage
Ec	Echert number
$E_{corrected}$	Corrected voltage
f	frequency
$\vec{F}$	force vector
g	Gravitational constant
$h_{alc}$	Height of alcohol
I	Current
L	Lift
$\dot{m}$	Mass flow
m	Mass
$P_{ava}$	Available kinetic energy in across rotor area
$P_{rot}$	Power extracted by the rotor
$p_\infty$	Ambient pressure
p	Pressure
$P_s$	Static pressure
$p_t$	Total pressure
Pr	Prantl number
Q	Torque
r	Radius
Re	Reynolds number
$R_{spec}$	Universal gas constant
R	Resistance
$R_{hw}$	Operating hot wire resistance
$R_{hw0}$	Hot wire resistance

R	Radius of rotor
Ri	Gross Richardson number
Ro	Rossby number
St	Strouhal number
T	Temperature
$T_{operate}$	Operating temperature of hot wire
$T_0$	Hot wire calibration temperature
t	Time [s]
TI	Turbulence intensity
T	Thrust force
TSR	Tip speed ratio
U	Free stream velocity
$U_R$	Velocity at rotor plane
$\Delta u_{max}$	Maximum velocity defect in wake
$U_{hub}$	Wind speed at hub height
u	Stream wise component of velocity
$\tilde{u}$	Fluctuating component of streamwise velocity
$\bar{u}$	Longitudinal component of Reynolds stress
$\bar{v}$	Horizontal component of Reynolds stress
$v_r$	Radial velocity component
$v_\theta$	Angular velocity component
v	Horizontal component of velocity
x	Streamwise axis
y	Horizontal axis
$y_{\frac{1}{2}}$	Half velocity point
z	Vertical axis

#### Greek

$\theta$	Angle [°]
$\theta$	Momentum thickness
$\Omega$	Angular velocity of the rotor
$\omega$	Rotational speed
$\rho$	Density of air
$\rho_{alc}$	Density of alcohol
$\alpha$	Angle of attac
$\psi$	Stream function
$\gamma$	Lapse rate
$\mu$	Dynamic viscosity
$\nu$	Kinematic viscosity for air (1.5e-5)





# 1 Introduction

The last couple of decades there have been an increasing interest in wind energy. Climate change, increasing energy demand and shortage of fossil energy sources have made alternative energy more popular than ever. Harnessing wind energy with horizontal axis wind turbines is a well established technology, and increasing interest call for more elaborate experimental data to predict and improve behavior of wind turbines. The wind turbine wake is of great importance when designing effective wind farms. Loss of momentum and increase in turbulence in the wake produce non ideal operating conditions for turbines operating in the wake of others. Turbines operating in the wake of others have reduced power output and higher wear on the blades, which reduce the overall economic output from a wind farm [3, 6].

It is of interest to map the wake behind a wind turbine to better understand the flow behavior and how it responds to different states of operation. How the wake from the tower and rotor interfere in the initial development of the wake and how far downstream it propagates before it disappears will be looked at in this paper. Streamwise velocity deficit, turbulence intensity and vortex shedding frequency in the wake of a cylinder and behind the operating wind turbine will be measured and analysed to map the development of the tower wake downstream of the wind turbine.

Some CFD studies looking at tower interference in the wake [28, 22] and full scale surveys of wakes behind operating wind turbines [18, 12] have been done earlier, but it has been difficult to find wind tunnel studies where the near wake of a wind turbine is studied with emphasis on the tower wake.

In a wind tunnel experiment it is not possible to obtain the same Reynolds number as a full-scale wind turbine will experience. This will cause some differences in the wind turbine characteristics, but the Reynolds number in the wake is considered to be sufficiently large to show the expected features of the wake, such as; wake rotation, tip vortices, and velocity deficit for similar drag coefficient.

In this paper, background on atmospheric conditions, classical theory on flow around cylinders, wind turbine operation, aerodynamics and experimental method will be presented. In the last part of the paper, experimental results from both a reference study on the wake of a smooth cylinder and the wake study behind an operating wind turbine will be given and discussed thoroughly.

## 2 Theory

### 2.1 The atmosphere

The atmosphere is a thin layer of gas covering the earth. It is divided in several layers with different characteristics, and the one with most relevance to us is the innermost layer called the troposphere. The troposphere is about 11km thick and contains most of the particles in the atmosphere. Clouds and weather exist only in this layer, and since there is little mixing with the outer layers of the atmosphere most of the pollution stays in this layer [4].

#### 2.1.1 The atmospheric boundary layer

The atmospheric boundary layer (ABL) is used to describe the lower layer of the troposphere which is directly affected by the temperature differences and friction from the surface. The top of the ABL is defined where the surface no longer has any influence on the wind speed. Smooth surfaces with a low friction coefficient and little generation of turbulence the ABL can be as thin as 200-300m, while over forests and big cities the ABL can be 600m or even thicker [13, 8, 4]. Wind turbines operate in this layer and the flow around them are affected by the varying atmospheric conditions.

**2.1.1.1 Stability** Pressure distribution in the troposphere can be described with the hydrostatic equation (1).

$$\frac{dP}{dz} = -\rho g \quad (1)$$

When a parcel of air moves upward in the atmosphere, the pressure of the surrounding air will decrease according to the formula. If we assume that air is an ideal gas, described with (2), both the temperature and density will decrease as the pressure decreases and the parcel expands. If we assume an adiabatic process, there is no heat exchange between the parcel of air and its surroundings and the enthalpy change (dH) in the first law of thermodynamics (3) is zero. Finally a relationship between temperature and height, the adiabatic lapse rate (4), can be derived from combining (3) and (1).

$$p = R\rho T \quad (2)$$

$$dH = \rho c_p dT - dP \quad (3)$$

$$\Gamma = \left( \frac{dT}{dz} \right)_{adiabatic} = \frac{g}{c_p} \quad (4)$$

The stability of the ABL is highly affected by the vertical temperature gradient, and can be divided in three different states: stable, neutrally stable, or unstable [13, 4]. Vertical variation in temperature and humidity give variation in density of the air. This vertical difference in density causes air to move up or down until it reaches equilibrium with the surrounding air. If this movement is accelerated, damped or non-existing determines the stability of the ABL.

$$\frac{dT}{dz} > \left( \frac{dT}{dz} \right)_{adiabatic} \quad (5)$$

In a stable ABL the temperature decreases slower, or even increases compared to the adiabatic lapse rate. A parcel of rising air will soon cool to a lower temperature than the surroundings and sink back until it reaches equilibrium. This can happen during night when the ground is cooler than the air above.

$$\frac{dT}{dz} < \left( \frac{dT}{dz} \right)_{adiabatic} \quad (6)$$

In an unstable ABL the temperature decreases faster than the adiabatic lapse rate. When hot air from the ground rises it cools slower than the air around it and accelerates upwards as the temperature difference increases. A typical example of an unstable atmosphere is on hot days with strong solar radiation which causes hot air to rise and as it cools down and condensation occurs it rises even faster forming towering cumulonimbus clouds.

$$\frac{dT}{dz} = \left( \frac{dT}{dz} \right)_{adiabatic} \quad (7)$$

When the temperature gradient in the ABL is equal to the adiabatic lapse rate the ABL

is neutrally stable. Air is in equilibrium with its surroundings and there is very little vertical motion. This state occurs when solar radiation is low, at high wind speed and well mixed ABL, and over bodies of water where surface temperature is less affected by solar radiation. For wind energy simulations, neutrally stable conditions are most often used.

## 2.1.2 Wind speed variation with height

The most accurate way to find the wind speed variation with height at a particular spot is to put up masts with anemometers and measure the wind speed over time. Since this is costly and time consuming, mathematical models have been developed to estimate the vertical wind profile. The most common models for meteorological and engineering purposes are the logarithmic model and the power law model. Wind speed near the ground is slowed by friction from the surface. Different terrain has different friction coefficients, and when using models to predict the wind speed it is necessary to take this into account.

**2.1.2.1 Roughness length** The roughness length describes the roughness of the terrain the wind is blowing. Surface roughness is an important variable which determines wind speed, turbulence intensity, scales of turbulence and the power spectrum of turbulence.  $z_0$  is the symbol used for roughness length, and it is found empirically by extrapolating values from wind profiles calculating the height where the wind speed is zero [4]. Tables for roughness length is given in several articles [8, 1, 7], and the one from Eurocode can be seen in table 1.

Because of changing wave height, the sea surface roughness length depends on the wind speed, distance from coast, and distance the wind has blown undisturbed over water, called the fetch [13]. Eurocode uses a  $z_0$  of 0.0003 [1] but there are several models which can be used to calculate the roughness length depending on friction velocity and fetch. Charnock proposed a model for calculating sea roughness length in 1955:

$$z_0 = \frac{a(u^*)^2}{g} \quad (8)$$

Where  $g$  is the gravitational constant,  $u^*$  the friction velocity and  $a$  the Charnock constant, assumed to be around 0.011 at open sea and between 0.016 and 0.02 in coastal areas [24].

<b>Terrain category</b>		$z_0$ [m]
0	Sea or coastal area exposed to open sea	0.003
I	Lakes or flata and horizontal area with negligible vegetation and without obstacles	0.01
II	Area with low vegetation such as grass and isolated obstacles (trees, buildings) with separations of at least 20 obstacle heights	0.05
III	Area with regular cover of vegetation or buildings or with isolated obstacles with separation of maximum 20 obstacle heights (such as villages, suburban terrain, permanet forrest	0.3
IV	Area in which at least 15% of the surface is covered with buildings and their average height exceeds 15m	1.0

Table 1: Terrain categories and corresponding roughness lengths in Eurocode [1]

**2.1.2.2 Logarithmic profile** The logarithmic profile (9) can be theoretically derived from several theories in fluid mechanics (mixing length theory, eddy viscosity theory, and similarity theory). It does not satisfy the no-slip condition which states that the wind speed is zero at the ground, it is also less accurate at higher altitudes with the area of application varying from 50m to 200m [8, 7]. It is often useful to represent the vertical wind speed compared to a measured wind speed at a reference height, then the  $u^*$  and  $\kappa$  cancel out and we get (10).

$$U(z) = \frac{u^*}{\kappa} \ln\left(\frac{z}{z_0}\right) \quad (9)$$

$$\frac{U(z)}{U(z_{ref})} = \frac{\ln\left(\frac{z}{z_0}\right)}{\ln\left(\frac{z_{ref}}{z_0}\right)} \quad (10)$$

$$u^* = \sqrt{\frac{\tau_0}{\rho}} \quad (11)$$

The friction velocity  $u^*$  is dependent on the shear stress  $\tau$  and the density of air  $\rho$ , the von Karman constant  $\kappa$  is usually 0.4,  $z_0$  the roughness length, and  $U_{ref}$  and  $z_{ref}$  is the reference wind speed at a given reference height, respectively.

**2.1.2.3 Power-law profile** The power-law profile (12) is a model developed empirically, and is widely used because of its simple mathematics. The power law does fulfill the no-slip condition, and has a better fit than the logarithmic profile at larger heights



and stronger winds [8].

$$\frac{U(z)}{U(z_{ref})} = \left(\frac{z}{z_{ref}}\right)^\alpha \quad (12)$$

$U_{ref}$  and  $z_{ref}$  is the same as in (10).  $\alpha$  can be found from empirical data, and depends heavily on the terrain but varies slightly with other parameters such as height, temperature and wind speed.

### 2.1.3 Turbulence

Turbulence is stochastic fluctuations of velocity, pressure and other variables in time and three dimensions. Kinetic energy in the wind is dissipated to thermal energy through creation and destruction of a cascade of smaller and smaller eddies. Large eddies feeds energy to smaller eddies which in term is destroyed by the viscosity and the energy dissipated as heat. Turbulent wind consist of a mean wind speed, usually measured over a period of 10 minutes, and a fluctuating wind speed, sampled at high frequencies, and given as a sum of these components in all three directions. In the longitudinal direction the instantaneous wind speed is  $u(z,t) = U + \tilde{u}$ , with  $U$  and  $\tilde{u}$  given by (13) and (14) [13, 4].

$$U = \frac{1}{\Delta t} \int_0^{\Delta t} u dt \quad (13)$$

$$\tilde{u} = \frac{1}{N} \sum_{i=0}^{N_s} u_i \quad (14)$$

Turbulence intensity(TI) is given by the standard deviation  $\sigma$  of the mean wind speed to the mean wind speed  $U$ , shown by (15) and (16).

$$I_U(z) = \frac{\sigma_U}{U(z)} \quad (15)$$

$$\sigma_U = \sqrt{\frac{1}{N_s - 1} \sum_{i=1}^{N_s} (u_i - U)^2} \quad (16)$$

An empirical formula for TI, using mean wind speed  $U(z)$ , height above ground  $z$  and roughness length  $z_0$ , is given by Eurocode [1]:

$$I_U(z) = \frac{1}{\ln\left(\frac{z}{z_0}\right)} \quad (17)$$

The TI is mainly dependent on the terrain but is affected by height and temperature differences.  $\sigma$  has been found to be dependent on the friction velocity  $u^*$  and is constant up to heights around 200m, above which it decrease [8]. Near ground the standard deviations for velocity in all three directions are given by:

$$\sigma_U = 2.5u^* \quad \sigma_V = 0.75\sigma_U \quad \sigma_W = 0.5\sigma_U \quad (18)$$

Since wind speed increases with height and  $\sigma$  is constant for a given  $u^*$ , TI must decrease with height according to (15) and increase with increasing surface friction (11). TI for typical operation conditions for wind turbines is in the range of 10-15% [2002].

## 2.2 Flow around a cylinder

Flow around cylinders is a well established area of study in fluid mechanics. The flow behaviour is highly dependent on the local Reynolds number which governs parameters such as boundary layer formation, drag coefficient, wake width and vortex shedding. For very low Reynolds numbers the flow will be steady and symmetrical, but as the Reynolds number increase the flow loses symmetry and an increasingly irregular wake develops behind the cylinder. At  $Re$  of around 35 von Karman vortex streets caused by periodic shedding of vortices from the back of the cylinder, appear in the wake. As the  $Re$  increase further the wake widens, and becomes turbulent between  $200 < Re < 400$ . The boundary layer on the cylinder is still laminar and separates on the windward side of the cylinder, the drag coefficient ( $C_d$ ) is around 1.0 to 1.2 and Strouhal number ( $St$ ) around 0.20. As  $Re$  reach a critical value around 300,000, depending on the free stream turbulence and roughness of the cylinder surface, the boundary layer becomes turbulent and stays attached to the surface to a point further back on the cylinder. This makes the wake narrower, and decreases the drag coefficient considerably [26, 11]. The huge drop in  $C_d$  is often called the "drag crisis" and figure 1 from [26], shows the relationship between  $Re$  and  $C_d$ .

$$Re = \frac{\rho U D}{\mu} \quad (19)$$

First part of this section will describe the simplified ideal flow around a cylinder followed by an introduction on viscous real life flow around a cylinder and wake flow theory. In the last part of the section, drag calculations based on pressure distribution on the cylinder surface and on the velocity defect in the wake will be shown.

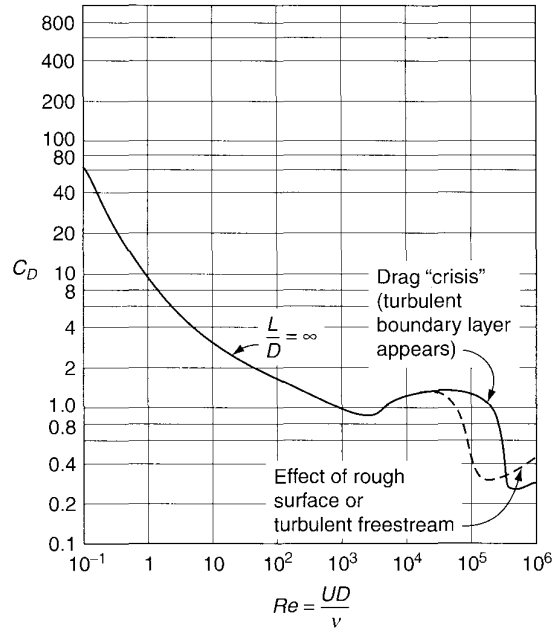


Figure 1: Relation between Reynolds number and drag coefficient [26]

## 2.2.1 Potential flow

**2.2.1.1 The stream function** To start with, the ideal flow around a cylinder is presented [5, 25, 26]. Steady, incompressible, irrotational, inviscid and 2-dimensional flow is assumed and we use the continuity equation:

$$\nabla \cdot \vec{U} = \frac{\partial u}{\partial x} + \frac{\partial v}{\partial y} = 0 \quad (20)$$

The continuity equation is satisfied if there exist a function  $\psi(x, y)$  so that:

$$\frac{\partial}{\partial x} \left( \frac{\partial \psi}{\partial y} \right) + \frac{\partial}{\partial y} \left( -\frac{\partial \psi}{\partial x} \right) = 0 \quad (21)$$

Evaluation of equations (20) and (21) show that the stream function  $\psi$  must be defined so that:

$$u = \frac{\partial \psi}{\partial y} \quad (22)$$

$$v = -\frac{\partial \psi}{\partial x} \quad (23)$$

This reduces the number of variables by one at the cost of increasing the derivatives by the order of one.

$$d\psi = \frac{\partial \psi}{\partial x} dx + \frac{\partial \psi}{\partial y} dy = -v dx + u dy = \vec{U} \cdot d\vec{A} = d\dot{m} \quad (24)$$

The equation above states that there is no mass flow,  $d\dot{m} = 0$ , across streamlines with constant  $\psi$  ( $d\psi = 0$ ).

As will be shown useful later, velocity components in cylindrical coordinates can be calculated from the stream function:

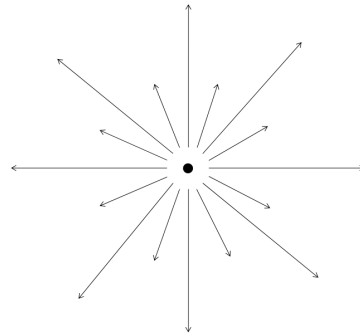
$$v_r = \frac{1}{r} \frac{\partial \psi}{\partial \theta} \quad (25)$$

$$v_\theta = -\frac{\partial \psi}{\partial r} \quad (26)$$

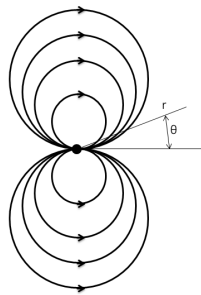
**2.2.1.2 Elementary flows** Equation (21) can be written as the Laplace equation:  $\nabla^2 \psi = 0$ . This means that the stream function is a linear second order partial equation, and that all equations that satisfy Laplace's equation can be combined to express complex flows. To describe the flow around a cylinder two elementary flows are combined: a *uniform flow* and a *doublet*. The uniform flow moves in a fixed direction at constant speed, with straight parallel streamlines everywhere in the flow field. A doublet is a combination of a *source* and a *sink* in a single point. Where the source has streamlines radially outwards from a fixed point in the center and sink streamlines inwards to a fixed point in the center. The streamlines in a doublet form circles above and below the center of the doublet, describing a circular flow with source and sink in the same point. Figure 2 show illustrations of the elementary flows mentioned above [5].



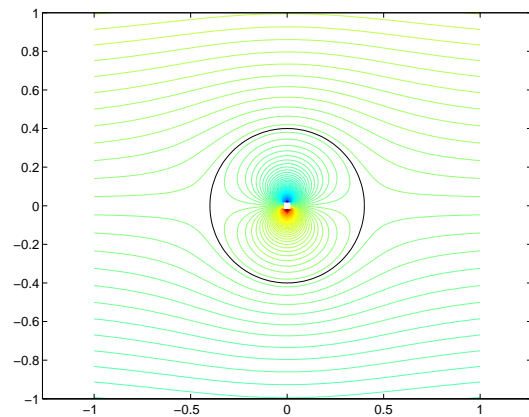
(a) Uniform flow



(b) Source



(c) Doublet



(d) Uniform + Doublet

Figure 2: Elementary flows

Stream functions for the uniform flow and doublet is, respectively:

$$\psi = Ursin\theta \quad (27)$$

$$\psi = -\frac{B}{r}sin\theta \quad (28)$$

So the combined stream function describing the flow around a cylinder becomes:

$$\psi = Ursin\theta - \frac{B}{r}sin\theta \quad (29)$$

Using equation (26) and (25) the tangential and radial velocity can be found from the stream function.

$$v_r = \frac{1}{r} \frac{\partial \psi}{\partial \theta} = U \cos \theta - \frac{B}{r^2} \cos \theta \quad (30)$$

$$v_\theta = -\frac{\partial \psi}{\partial r} = -U \sin \theta - \frac{B}{r^2} \sin \theta \quad (31)$$

As shown in equation (24), there is no velocity normal to a streamline, and this can be used for the streamline at  $r = R$ , where  $R$  is the radius of the cylinder.  $v_r = 0$  when  $r = R$  gives  $B = R^2 U$ , and the constant  $B$  can be omitted from equation (31) and (30):

$$v_r = U \cos \theta \left(1 - \frac{R^2}{r^2}\right) \quad (32)$$

$$v_\theta = -U \sin \theta \left(1 + \frac{R^2}{r^2}\right) \quad (33)$$

Now the velocity-field around the cylinder is expressed as a function of distance from the center  $r$  and angular position  $\theta$ . The highest velocity is found at the cylinder surface at top and bottom of the cylinder,  $r = R$  and  $\theta = \pi/2$  or  $3\pi/2$ . This violates the no-slip condition imposed by intermolecular forces between the surface and the fluid just above it, and shows that ideal flow is just an approximation to the real life problem. At the front and back of the cylinder,  $\theta = \pi$  or  $0$ , the velocity is zero and these points are called stagnation points [5, 26].

### 2.2.2 Viscous flow around a cylinder

Ideal flow is a huge simplification to make flows easier to work with but a lot of information is lost. The flow around a cylinder in figure 2d show smooth streamlines and only a small boundary-layer close to the cylinder. Ideal flow is not governed by the physical properties which real life flows are determined by. The viscous forces cause the flow to separate from the cylinder and create a wake behind it. An actual flow around a cylinder would look somewhat like the sketch in figure 4 if  $Re$  is subcritical, and 3 if  $Re$  is supercritical/transcritical.

As shown in figure 1 presence of free stream turbulence lower the critical Reynolds number, and a highly turbulent free stream will hasten transition to turbulent boundary layer on the cylinder surface and hence delay separation [20, 26]. For Reynolds number

above  $\approx 400$  the viscous flow around a cylinder produces a turbulent stochastic wake behind the cylinder which will be addressed in the next section.

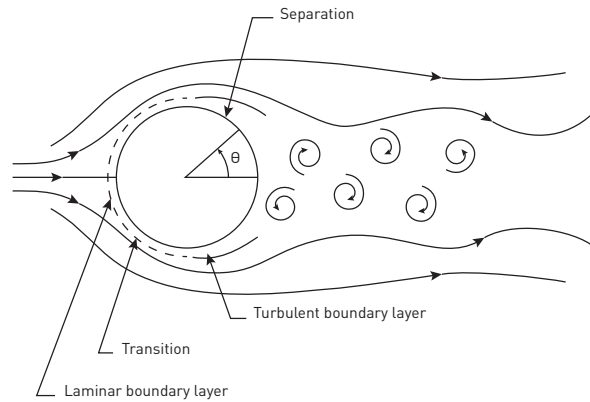


Figure 3: Turbulent/high Reynolds number flow around a cylinder

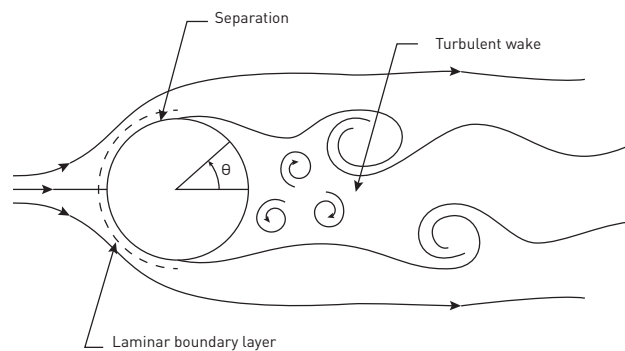


Figure 4: laminar/low Reynolds number flow around a cylinder

### 2.2.3 Wake theory

Behind a bluff body submerged in a moving fluid, there will for  $35 < Re < 10^7$  be shed vortices from the back of the cylinder, periodically alternating between the left and right side. The array of vortices created behind the cylinder is called a von Kármán vortex street, after Theodore von Kármán. The dimensionless shedding frequency is given by the *Strouhal number* in equation (34), and stays constant over a wide range of Reynolds numbers. Behind a circular cylinder the Strouhal number is equal to around 0.2 for Reynolds numbers between 100 and  $10^5$ , as can be seen in figure 5. The theory and equations presented in this section is gathered from several references ([23, 26, 27]) and will not be referred to continuously.

$$St = \frac{fD}{U} \quad (34)$$

Here  $f$  is the shedding frequency,  $D$  diameter of the cylinder, and  $U$  the free stream velocity.

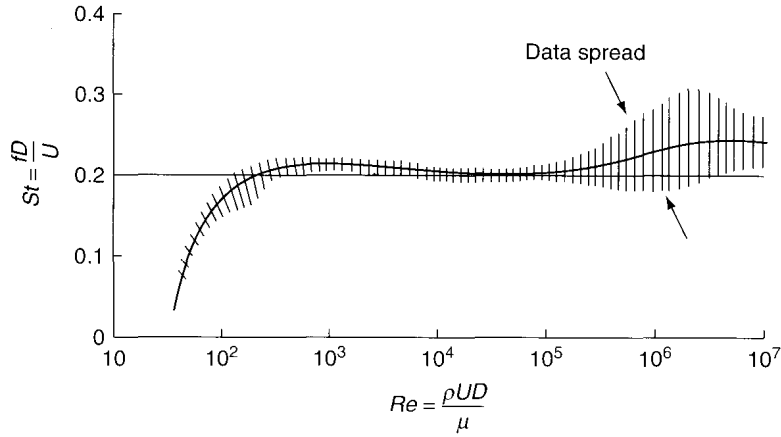


Figure 5: Strouhal number as a function of Reynolds number behind a circular cylinder [26]

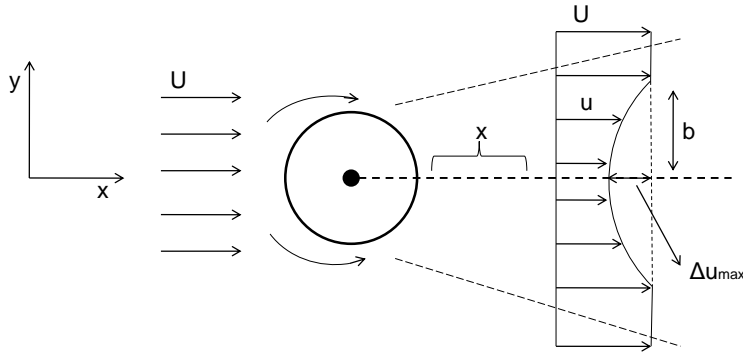


Figure 6: Sketch of wake behind cylinder, showing key variables

In figure 6 a sketch of the velocity defect in the wake of a cylinder is shown.  $\Delta U_{max}$ ,  $b$  and  $x$  are maximum velocity defect, wake half-width and distance downstream of the cylinder, respectively. Far downstream of the cylinder the wake is assumed to become self-similar:

$$\frac{\Delta u}{\Delta u_{max}(x)} = fcn\left[\frac{y}{b(x)}\right] \quad (35)$$



Equation (36) show the momentum integral for a plane wake, and show that the drag force  $F$  found from the wake profile is independent of  $x$ .

$$F = \int_{-\infty}^{+\infty} \rho \bar{u} \Delta u dA = const \approx (const) \rho U \Delta u_{max} b \quad (36)$$

The last term of equation (36) is true if the velocity defect is assumed to be small,  $\Delta u \ll U$ . For the equation to be independent of  $x$   $\Delta u_{max} \propto b^{-1}$

Stream wise momentum equation:

$$u \frac{\partial u}{\partial x} + v \frac{\partial u}{\partial y} + \frac{\partial}{\partial y} (\bar{u}^2 - \bar{v}^2) + \frac{\partial}{\partial y} (\bar{u}\bar{v}) = \nu \left( \frac{\partial^2 U}{\partial x^2} + \frac{\partial^2 U}{\partial y^2} \right) \quad (37)$$

When looking at the order of magnitude, the viscous fifth term can be neglected if the Reynolds number is sufficiently large. The third term is negligible far downstream of the object. Since  $u \gg v$  the second term is neglected and equation (37) become:

$$u \frac{\partial u}{\partial x} + \frac{\partial}{\partial y} (\bar{u}\bar{v}) = 0 \quad (38)$$

Sufficiently far downstream the fluctuating velocity components  $\bar{u}$  and  $\bar{v}$  is proportional to the velocity defect  $\Delta u_{max}$ , and because of the small velocity defect  $u \frac{\partial u}{\partial x} \approx U \frac{\partial u}{\partial x}$ .

With  $\xi = (\frac{y}{b})$ , order-of-magnitude analysis gives the following:

$$U \frac{\partial u}{\partial x} = U \left( -\frac{d\Delta u_{max}}{dx} f + \frac{\Delta u_{max}}{b} \frac{db}{dx} \xi f' \right), \quad (39)$$

$$\frac{\partial}{\partial y} (\bar{u}\bar{v}) = -\frac{\Delta u_{max}^2}{b} g'$$

With the relations in (39), equation (38) becomes:

$$-\frac{Ub}{\Delta u_{max}^2} \frac{d\Delta u_{max}}{dx} f + \frac{U}{\Delta u_{max}} \frac{db}{dx} \xi f' = g' \quad (40)$$

For universal shapes of  $f$  and  $g$  so that the normalised velocity and Reynolds stress profiles are the same at all  $x$ , the coefficients of  $f$  and  $\xi f'$  in equation (40) must be constant. The free stream velocity  $U$  is also constant and we need to solve for:

$$-\frac{b}{\Delta u_{max}^2} \frac{d\Delta u_{max}}{dx} = const, \quad (41)$$

$$\frac{1}{\Delta u_{max}} \frac{db}{dx} = const$$

The solution to (41) is  $b \sim x^n$  and  $\Delta u_{max} \sim x^{n-1}$ . For the momentum integral in equation (36) to be constant  $x^n x^{n-1} = const$ ,  $2n - 1 = 0$ , so that  $n = \frac{1}{2}$ . This means that self-similarity cannot be achieved unless:

$$b = const x^{\frac{1}{2}}, \quad (42)$$

$$\Delta u_{max} = const x^{-\frac{1}{2}}$$

Using the Clauser-type eddy-viscosity distribution from equation (43) and taking  $b$  as the half-velocity point  $y_{\frac{1}{2}}$ , the solution of the self similar velocity-defect profile become as shown in (44).

$$\mu_t(jet) \approx K\rho U_{max} b = const x^{\frac{1}{2}} \quad (43)$$

$$\frac{\Delta u}{\Delta u_{max}} \approx \exp\left(\frac{-0.693y^2}{y_{\frac{1}{2}}^2}\right) \quad (44)$$

To calculate the variations in  $\Delta u_{max}$  and  $y_{\frac{1}{2}}$  the constants in (42) must be determined by experiments. Wygnanski did measurements in the wake of several objects and found them to be 0.275 and 1.75 for  $b$  and  $\Delta u_{max}$ , respectively, which give the following growth-rates:

$$y_{\frac{1}{2}} \approx 0.275(x\theta)^{\frac{1}{2}}, \quad (45)$$

$$\Delta u_{max} \approx 1.75U\left(\frac{\theta}{x}\right)^{\frac{1}{2}}$$

With the momentum thickness  $\theta$ :

$$\theta = \int_{-infly}^{+\infty} \frac{\Delta u}{U} \left(1 - \frac{\Delta u}{U}\right) dy = const \quad (46)$$

For estimation of theta from D and expected  $C_d$  equation (47) is used [25].

$$\theta = \frac{C_d D}{2} \quad (47)$$

#### 2.2.4 Drag and drag coefficient

Drag on any object can have two sources: form drag (pressure drag), from the pressure difference fore and aft of the object; and friction drag, caused by the shear stress from the moving fluid particles on the surface of the object. The distribution between them relies very much on the shape of the body. For an infinitely thin flat plate 100% of the drag force comes from friction. As the shape of a body thickens, more and more of the total drag force can be attributed to the pressure drag. Friction drag on a cylinder is only about 3% of the total drag, while the rest is pressure drag [25]. Newton's second law states that the net force acting on a particle is equal to the time rate of change of the linear momentum of the particle. In a steady and irrotational coordinate system the force vector can be written as:

$$\vec{F} = \frac{\partial}{\partial t}(m\vec{U}) \quad (48)$$

Using *Reynolds transport theorem*:

$$\frac{dB}{dt} = \frac{d}{dt} \int_{CV} \frac{dB}{dm} \rho d(vol) + \int_{CS} \frac{dB}{dm} \rho \vec{U} \cdot d\vec{A} \quad (49)$$

Where B is equal to the linear momentum  $m\vec{U}$  the integral form of the linear momentum becomes:

$$\vec{F}_{body} + \vec{F}_{surface} = \frac{\partial}{\partial t} \int_{CV} \rho \vec{U} d(vol) + \int_{CS} \vec{U} (\rho \vec{U} \cdot \hat{n} dA) \quad (50)$$

The forces acting on a particle can be divided in *volumetric*, or *body* forces and *surface* forces. Body forces include gravity, electric and magnetic forces while surface forces comprise pressure and viscous forces. Only the surface forces in the stream wise direction (here assumed to be x) contribute to the drag on a cylinder so the body forces can be [14, 26]. On integral form the steady state momentum equation looks like:

$$\vec{F}_{surface,x} = -d = \int_{CS} u(\rho \vec{U} \cdot dA) \quad (51)$$

For any object in a fluid, the drag coefficient  $C_d$  is a nondimensional relationship between drag force on the object per area and the dynamic force in the fluid over that area:

$$C_d = \frac{d}{\frac{1}{2}\rho U^2 A} \quad (52)$$

Drag coefficient per unit span of a cylinder with radius R is:

$$C_d = \frac{d}{\frac{1}{2}\rho U^2 2R} \quad (53)$$

**2.2.4.1  $C_d$  from velocity deflection in wake** Drag of a cylinder can be calculated from the velocity deficit in the wake. If one assumes constant  $\rho$  in equation (51) the drag per unit span can be simplified to:

$$d = \rho \int_0^y u(U - u) dy \quad (54)$$

Where  $y$  is the span of the wake,  $U$  the free stream velocity and  $u$  the local velocity in the wake. Linear approximation gives:

$$d \approx \sum u(U - u)\Delta y \quad (55)$$

Using equation (53) and (54) the result is an expression for the drag coefficient using the velocity deficit in the wake:

$$C_d = \frac{1}{\frac{1}{2}U^2 2R} \sum u(U - u)\Delta y \quad (56)$$

**2.2.4.2  $C_d$  from pressure distribution on cylinder** The Bernoulli equation (82) states that the total pressure is the sum of static pressure and the velocity. Since the velocity on the surface of a cylinder is dependent on  $\theta$  (see section 2.2.1) the local static pressure can also be expressed as a function of  $\theta$ :

$$p = p_\infty + \frac{1}{2}\rho U^2 - 2\rho U^2 \sin^2 \theta \quad (57)$$

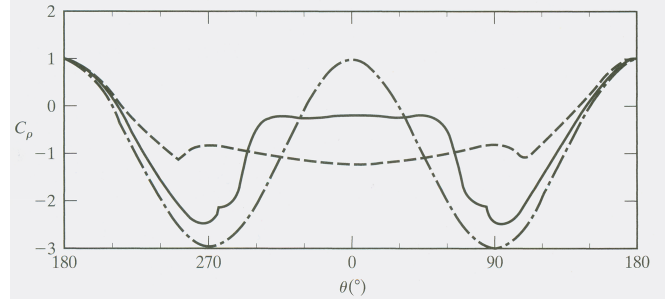


Figure 7:  $C_p$  distribution on a cylinder for ideal flow (dash-dot-line), subcritical Reynolds number (dashed line) and supercritical Reynolds number (solid line) [5]

Where  $p$  is the total pressure,  $p_\infty$  the static pressure and  $U$  the free stream velocity. Expressing the pressure distribution on a cylinder with the dimensionless parameter  $C_p$ , obtained with equation (58), it looks like in equation (59).

$$C_p = \frac{p - p_\infty}{\frac{1}{2}\rho U^2} \quad (58)$$

$$C_p = 1 - 4\sin^2\theta \quad (59)$$

With a known pressure distribution on the cylinder surface, the drag force acting on it can be found by integrating the pressure forces acting in the stream wise direction:

$$d = - \int_0^{2\pi} p \cos\theta R d\theta \quad (60)$$

Using  $p$  from equation (57):

$$d = - \int_0^{2\pi} (p_\infty + \frac{1}{2}\rho U^2 - 2\rho U^2 \sin^2\theta) \cos\theta R d\theta \quad (61)$$

This will give  $d = 0$ , known as d'Alembert's paradox. In real, viscous flow, the flow will separate from the cylinder and the pressure distribution around the cylinder will depend on the Reynolds number as in figure 7 and be quite different than for ideal potential flow. The pressure on the front of the cylinder will be considerably higher than in the separated region behind the cylinder, and cause a drag force in the streamwise direction [5].

Using equation (58) it is possible to reduce equation (61) to:

$$d = -\frac{1}{2}\rho U^2 R \int_0^{2\pi} C_p \cos \theta d\theta \quad (62)$$

Putting the above expression into equation (53) and assuming 0 friction drag, the drag coefficient becomes:

$$C_d \approx -\frac{1}{2} \int_0^{2\pi} C_p \cos \theta d\theta \quad (63)$$

Linear approximation gives:

$$C_d \approx -\frac{1}{2} \sum_{\theta=0}^{2\pi} C_p(\theta) \cos \theta \Delta\theta \quad (64)$$

## 2.3 Wind turbine aerodynamics

### 2.3.1 Theoretical power production

It is possible to estimate the power production of a wind turbine by one-dimensional momentum theory, considering the stream tube in figure 8 with mass and momentum conservation over the control volume. The rotor plane can be simplified with a porous disc creating the desired pressure drop across the rotor plane. As the wind approach the disc velocity drops and pressure increase to  $p_{R1}$  on the windward side of the disc according to the Bernoulli equation (88). Over the disc the pressure drop to  $p_{R2}$  directly after the disc, where it start to increase and reach ambient pressure  $p_\infty$  far downstream. The pressure difference between  $p_{R1}$  and  $p_{R2}$  give the force acting on the disc [15, 13, 10].

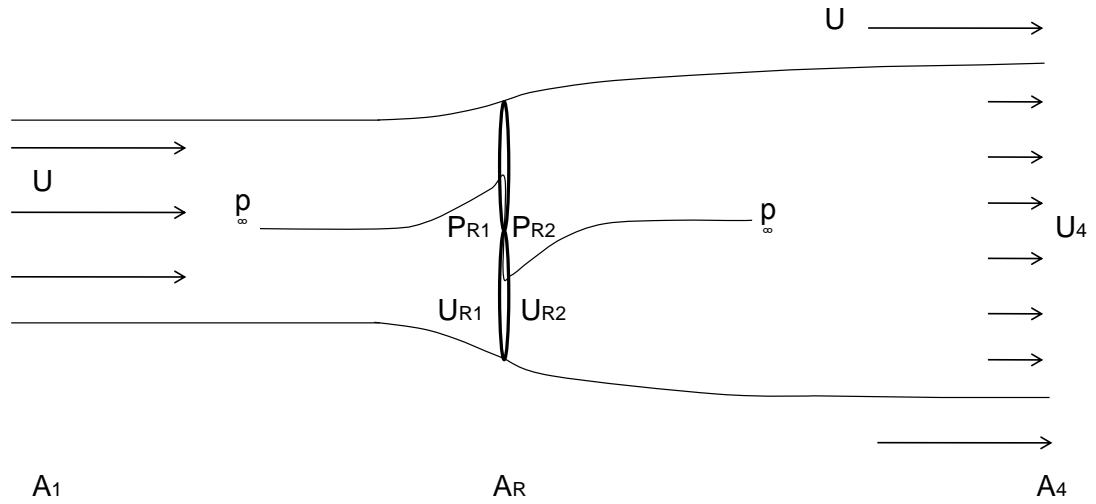


Figure 8: Illustration of flow through a wind turbine using 1D momentum theory

Using inflow and outflow conditions such that the pressure is  $p_\infty$  one can use the momentum balance over the stream tube in figure 8 to estimate the theoretical power output. The mass flow through the stream tube is:

$$\dot{m} = \rho A_1 U = \rho A_4 U_4 = \rho A_R U_{R1} \quad (65)$$

Where the subscripts 1, 4 and R1 specify the positions far upstream of the wind turbine, far downstream of the wind turbine and the rotor plane, respectively. The thrust force becomes:

$$T = \dot{m}U - \dot{m}U_4 = \rho A_1 U^2 - \rho A_4 U_4^2 \quad (66)$$

Using Bernoulli upstream and downstream of the turbine the pressure difference over the rotor plane can be expressed as:

$$p_{R1} - p_{R2} = \frac{1}{2} \rho (U^2 - U_4^2) \quad (67)$$

Using equation (67) the thrust can be written as a function of the rotor area  $A_R$ , free stream velocity  $U$  and the wake velocity  $U_4$ :

$$T = \rho A_R (U^2 - U_4^2) \quad (68)$$

With equations (68), (66) and  $\dot{m} = \rho A_R U_{R1}$  one can find that the  $U_{R1}$  is the average of free stream and wake velocity:

$$U_{R1} = \frac{U + U_4}{2} \quad (69)$$

Defining an axial induction factor  $a$  as the fractional slow down in wind velocity from free stream to rotor plane one can express both  $U_{R1}$  and  $U_4$  in terms of  $U$  and  $a$  [13].

$$a = \frac{U - U_{R1}}{U}$$

$$U_{R1} = U(1 - a) \quad (70)$$

$$U_4 = U(1 - 2a)$$

The power extracted by the wind turbine can now be expressed as:

$$P = \frac{1}{2} \rho A_R U^3 4a(1 - a)^2 \quad (71)$$

Available kinetic energy in the wind across the rotor area is given by:

$$P_{ava} = \frac{1}{2} \rho U^3 A_R \quad (72)$$

Where  $U$  is wind velocity perpendicular to the rotor plane,  $A_R$  the area swept by the turbine blades, and  $\rho$  the density of air. The ratio of power extracted by the wind turbine to the power available is called the power coefficient  $C_P$ , and is the common way to express wind turbine performance. Using equations (71) and (72) the  $C_P$  becomes:

$$C_P = \frac{P}{P_{ava}} = 4a(1 - a)^2 \quad (73)$$

If all the kinetic energy in the wind was extracted by the turbine, the velocity would be zero behind the rotor and mass would build up, which is not possible. Since the air downstream of the turbine need some energy to move away ( $U_{R2} \neq 0$ ) there exist a maximum aerodynamical efficiency of a wind turbine called the Betz limit. To find the maximum induction factor one have to take the derivative of equation (73) with respect



to  $a$ , obtaining  $a_{max} = \frac{1}{3}$ . Using this in equation (73) the Betz limit can be calculated:

$$C_{P,max} = \frac{16}{27} = 0.5926 \quad (74)$$

The thrust on a wind turbine can also be expressed as a non-dimensional thrust coefficient  $C_T$ , which gives ratio of thrust force experienced by the wind turbine to the dynamic force in the wind across the rotor area. By using equation (68) and the induction factor from (70), the thrust experienced by the rotor becomes:

$$T = \frac{1}{2}\rho A_R U^2 4a(1-a) \quad (75)$$

$$C_T = \frac{T}{\frac{1}{2}\rho U^2 A_R} \quad (76)$$

With the axial induction factor  $a = \frac{1}{3}$ ,  $C_{T,max}$  becomes  $\frac{8}{9}$ .

Together with the actual wind from the environment  $U_R$ , the blades of a wind turbine experiences an induced wind  $\Omega R$  parallel to the blades due to the rotation itself, see figure 9. The wind speed and direction seen by the blade is a combination of these factors, and creates a torque  $Q$  on the blades.

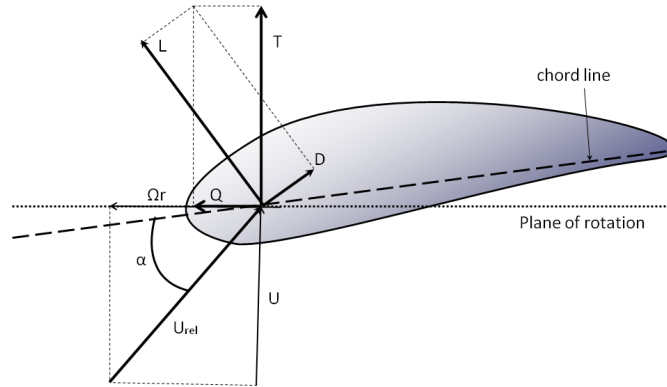


Figure 9: Wind speed, angle of attack and forces on a blade element

By measuring the torque and the angular velocity on an operating wind turbine the actual power extracted by the rotor can be calculated from ( $P_{rot} = Q\omega$ , and the aerodynamical efficiency is given by (77).

$$C_P = \frac{P_{rot}}{P_{ava}} = \frac{Q\omega}{\frac{1}{2}\rho U^3 A_R} \quad (77)$$

The tip speed ratio TSR is the ratio between the tip speed of the rotor and the free stream wind speed:

$$TSR = \frac{\Omega R}{U} \quad (78)$$

As the rotational speed of the rotor increase compared to the free stream wind speed, the TSR increases and the relative wind seen by the blades change toward a more tangential direction. The angle of attack  $\alpha$  change and as seen in figure 11 the lift and drag coefficients change. At low TSR the blade experience a high angle of attack, which decreases as the TSR increase

**2.3.1.1 Aerodynamics of the airfoil** The blades are shaped like wings on an airplane and its main function is to create highest possible lift-force with the least amount of drag. Lift is generated by the difference in dynamic pressure that arises when the airflow on the upper side is forced to travel at higher speed than air below the airfoil. Drag forces have two sources; skin friction along the surface and pressure drag due to the difference in pressure force between leading and trailing edge. At normal operation the wake behind the airfoil is small and skin friction is the main cause of drag. Lift and drag forces depend on the airfoil shape and roughness, angle of attack, turbulence level, and Reynolds number and equations for both are given below:

$$L = \frac{1}{2}\rho U^2 C_l \quad (79)$$

$$D = \frac{1}{2}\rho U^2 C_d \quad (80)$$

As seen in figure 11 the lift and drag coefficients for a given airfoil,  $C_l$  and  $C_d$  respectively, depend on the turbulence level and angle of attack. At higher angles of attack the airflow over the airfoil are no longer able to follow the shape of the airfoil and separates, or stalls as in figure 10. The pressure in the stalled region is higher than the pressure of the attached flow, decreasing the pressure difference between upper and lower side and hence the lift force on the airfoil. When the flow separates the size of

the wake behind the airfoil also increases dramatically and the difference in pressure force between leading and trailing edge increases. This causes higher  $C_d$  and higher drag force on the airfoil.

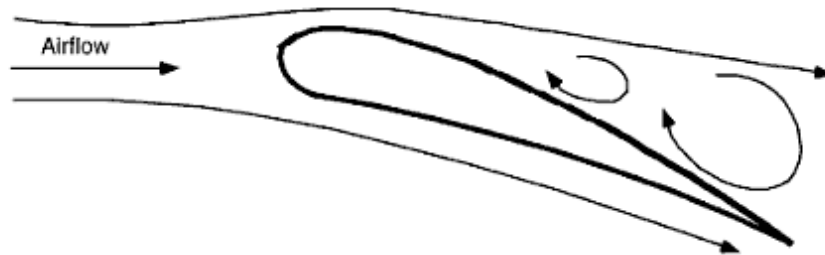


Figure 10: Stalled airfoil [13]

In turbulent wind conditions the transition point from laminar to turbulent boundary layer move towards the leading edge of the airfoil and at high levels of turbulence the whole boundary layer may be turbulent. A turbulent boundary layer is thicker, contains more energy, and increase friction drag on the surface, compared to a laminar boundary layer. Higher energy in the boundary layer delays stall and enables the airfoil to produce lift at higher angles of attack. Higher skin friction increase surface drag and a thicker boundary layer increase the pressure drag [5, 9].

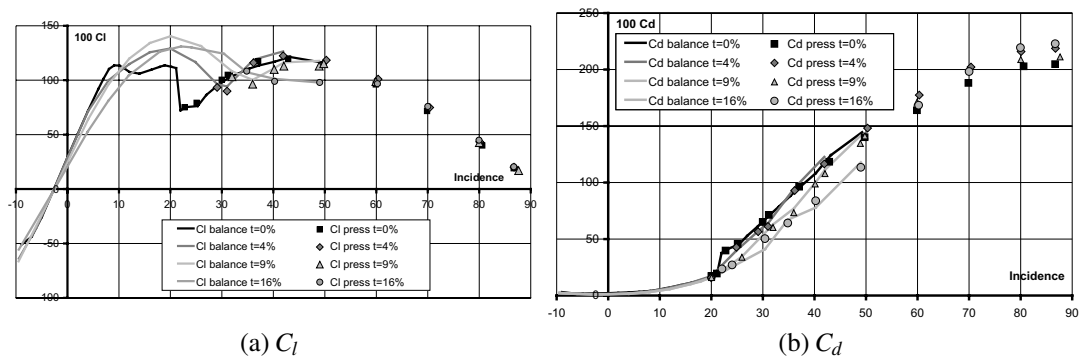


Figure 11:  $C_l$  and  $C_d$  vs  $\alpha$  for airfoil operating at different levels of turbulence with  $Re=400,000$  [9]

### 2.3.2 Wind Turbine Wakes

Due to the loss of momentum through thrust force on the wind turbine, a wake region with decreased velocity will form behind it. To satisfy the Bernoulli equation the flow area must expand behind the rotor. At the edges of the wake a boundary layer will

form between the turbulent wake flow and the flow outside. As the wake propagates downstream, the surrounding air will mix with the wake adding momentum to the wake and causing the velocity defect to decrease and the wake to expand further. As for the wake behind a cylinder, or any immersed body, the wake will reach a self similar profile far downstream. Experiments show that self similar profiles are reached at distances of the order of  $x=30D$  [15]. As for the wake behind a disc normal to the stream vortex streets will form in the wake of a wind turbine as well [17]. Experiments show that the Strouhal number behind a wind turbine will approach that of a disc as the solidity in the swept area increases for higher TSR. Tip vortices and vortices behind the nacelle and tower will also form, making the wake flow even more complex. When plotting the power spectrum density (psd) of the wake, the three blades passing are expected to show up at 3 times the rotation frequency.

**2.3.2.1 Wake rotation** The forces driving the wind turbine blades are also felt by the air moving over the airfoil, but in the opposite direction. This cause the wake to rotate in the opposite way of the turbine rotor [10, 13]. Since the air experience the same torque as the rotor, turbines operating at low TSR with high torque will have a higher loss of kinetic energy to the wake turbines operating at high TSR with low torque. Thus the wake behind a turbine operating at high torque will rotate faster than the wake behind a turbine operating at low torque.

$$dP = \dot{m}\omega r C_{\theta} dr = 2\pi r^2 \rho u \omega r C_{\theta} dr \quad (81)$$

$C_{\theta}$  is the azimuthal velocity of the air in the wake caused by the force from the turbine blades. For a given power and free stream velocity, the azimuthal velocity in the wake decrease with increasing rotational speed  $\omega$ . This means that it is more efficient to operate a wind turbine at high TRS and thereby low angle of attack,  $\alpha$ , to minimize the loss of kinetic energy in the rotating wake.

**2.3.2.2 Turbulence intensity** Vortex streets behind the blade roots/nacelle and tip of the blades propagate downstream and cause a higher TI in these areas. Especially at the tips the TI will be higher, with a flatter TI profile in the middle of the wake. Also just downstream of the turbine a higher TI in the wake center is expected due to the tower wake. This area of increased TI is expected to fade out rather quick due to the heavy mixing in the wake.

**2.3.2.3 Expected tower influence** Behind the rotor of the wind turbine the flow will be highly turbulent and critical Reynolds number for flow around the tower will be lower than for non-turbulent flow. As shown in figure 1 the high free stream turbulence experienced by the tower will affect the boundary layer flow and separation point and the wake behind the tower will be narrower than for a cylinder in a non turbulent flow of similar Reynolds number [20, 26].

## 3 Experimental set-up

### 3.1 Instruments and facilities

The large wind tunnel in the fluids engineering lab at The Norwegian University of Science and Technology was used for the experimental work. It operates on a closed circuit and is 2.7m wide, 11m long and 1.8m high after the contraction increasing to 2m at the end. A model wind turbine with hub-height of 0.87m, rotor diameter ( $D_R$ ) of 0.85m and tower diameter ( $D$ ) of 0.12m were used in the experiments. For the reference experiment on the wake of a circular cylinder, a smaller open-jet wind tunnel with a 1m long, 0.45m wide and 0.45m high test section was used. The cylinder used had a diameter of 0.025m and 16 pressure taps evenly placed around its circumference. Pitot tubes and hot wires were used for anemometry.

The Pitot tubes were connected to a pressure transducer and an amplifier. The hot wire was connected to an anemometer and an amplifier. To obtain the correct free stream wind speed when the model turbine was operating, the pressure difference over the contraction ahead of the wind tunnel test section was used. A scale was used to measure thrust on the model turbine, and a torque meter measured the torque on the turbine blades.

Rotational speed of the model turbine was recorded using reflective tape at one of the blades and recorded by a tachometer. There is also a build in photovoltaic cell in the nacelle of the model turbine which was connected to an oscilloscope to double check the easier obtainable measurements from the tachometer.

Pitot tube and hot wire measurements 90000 samples were taken over 30 seconds at 3000Hz. For the hot wire measurements a filter for frequencies at 1000Hz were used. Torque, thrust and reference wind speed measurements were sampled at 500Hz for 15 seconds giving 7500 samples. The data were collected with a National Instruments NI cDAQ-9172. LabView was used to control, observe and log the measurements on a PC. Time series from the hot wire measurements were converted to turbulence info with an in house developed FORTRAN script. Another FORTRAN script was used for the spectral analysis.

### 3.1.1 Calibration

**3.1.1.1 Pitot** The pressure transducers were calibrated using a fluid column manometer. Height of fluid and corresponding voltage from the NI cDaq-9172 was collected with the fan operating at different rotational speeds. Bernoulli's equation states that the stagnation pressure, or total pressure, ( $p_t$ ) equals the sum of static ( $p_s$ ) and dynamic pressure ( $\frac{1}{2}\rho U^2$ ).

$$p_t = p_s + \frac{1}{2}\rho U^2 \quad (82)$$

Assuming that the density is constant throughout the column of fluid, one can use the simplified hydrostatic equation, where  $\rho_{alc}$  and  $h$  gives the density and height of the fluid respectively. The density of the fluid was not calibrated but was assumed to be  $800 \frac{kg}{m^3}$  and the gravitational acceleration supposed to be  $9,82 \frac{m}{s^2}$ .

$$p = \rho_{alc} g h_{alc} \quad (83)$$

By combining (82) and (83) the velocity can be found:

$$U = \sqrt{\frac{2\Delta p}{\rho}} \quad (84)$$

A calibration curve was obtained by doing a linear regression on the plotted dynamic pressure against the corresponding voltage, and the relationship was found.

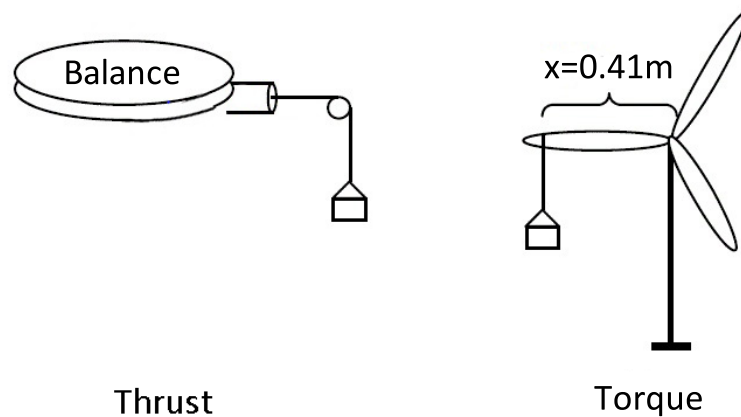


Figure 12: Calibration of thrust and torque (modified from [6])

**3.1.1.2 Thrust and torque** When calibrating the scales for thrust and torque a set of known weights were used as in figure 12 and plotted against the voltage, the calibration curves were obtained in the same way as for the pitot.

**3.1.1.3 Hot wire** The resistance of a hot wire is dependant of temperature. In this case was the hot wire operational temperature set to 320° C. Fluctuations in wind speed cause variations in the mass flow of air past the hot wire, and thus variations in the heat exchange between wire and air. Since the hot wire is set to operate at a constant temperature, the electric current through the wire must be adjusted when the temperature and hence resistance changes. The wind speed fluctuations are converted to a changing electric signal. Ohms law states:

$$E = RI \quad (85)$$

Resistance in the hot wire is set by:

$$R_{tot} = R_{cable} + R_{hw0}(1 + \underline{\alpha\Delta T}) \quad (86)$$

$R_{tot}$  is the total resistance of the hot wire with cable and holder at the given operating temperature.  $\alpha$  and  $R_{hw0}$  depends on the hot wire itself and given to be 1.69e-3 and 6.0Ω respectively.  $\Delta T = T_{operate} - T_0$  is the difference between the operating temperature of hot wire  $T_{operate}$  and the calibration temperature  $T_0$ .  $R_{cable}$  was measured to 1.1Ω and  $\Delta T$  was set to 300°C for calculating the onset resistance from the anemometer.

The underlined part of equation (86) can be set by the anemometer to obtain the desired operating temperature from 0.5 and increasing with increments of 0.1.  $\alpha \Delta T = 0.507$  so 0.5 was chosen on the anemometer which gives a operating temperature between 315°C and 324°C with ambient temperatures ranging from 20°C to 29°C.

Since the hot wire works by keeping temperature constant, it is very sensitive to temperature change in the airflow. It is desirable to calibrate the hot wire at a constant temperature so the temperature at the first and last calibration point does not deviate. This is not possible since the temperature in the wind tunnel changes quite a bit during operation and this have to be corrected for in the later measurements. Temperature is logged for each measurement in the calibration and corrected with the temperature from the first measurement.



$$E_{corrected} = E \sqrt{\frac{T_{operate} - T_0}{T_{operate} - T}} \quad (87)$$

Where  $T_0$  is the calibration temperature at the first calibration point,  $T_{operate}$  the operating temperature of the wire, and  $T$  the actual temperature.

The hot wire was calibrated for each series of measurements. An example of the hot wire calibration curve can be found in the appendix A, with the calibration curves for Pitot, torque and thrust.

### 3.2 Reference experiment - wake behind a cylinder

Wake measurements behind a cylinder are done to get acquainted with the measuring techniques and instruments, and the results gathered will be a good indication on what to expect behind the tower of the model wind turbine later on. The cylinder has a blockage ratio of around 5%, which is expected to have very little impact on the results [21].

A hot wire and a Pitot tube are mounted on a traverse fixed to a free-standing structure as an effort to minimize disturbance from the wind tunnel fan, causing the wind tunnel to vibrate. The probes are lowered into the center of the test section through a slit in the top cover of the wind tunnel. With the probes at cylinder height the height scale on the traverse is set to zero, allowing to control the measuring height accurately in relation to the middle of the cylinder. Velocity and turbulence data will be gathered for three cases; empty tunnel,  $x = 4.5D$  diameters and  $x = 8.5D$ .

With wind speed around  $10 \frac{m}{s}$  the Reynolds number obtained is in the range of  $10^4$ . This is of course several orders lower than what the tower of a HAWT experience, and will probably cause earlier flow separation on the cylinder surface due to the low turbulence and Reynolds number, hence a broader wake. The low Reynolds number and turbulence may also affect the vortex shedding which is expected to be found behind the cylinder.

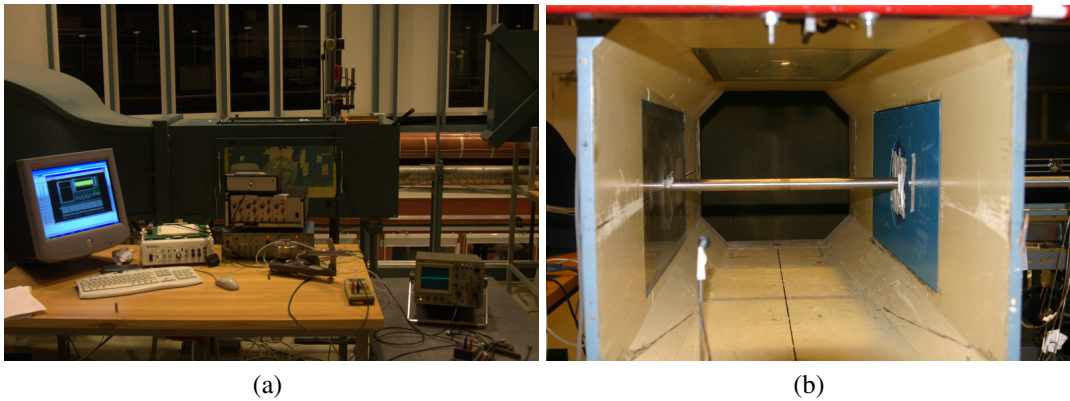


Figure 13: The wind tunnel set-up and cylinder used in reference experiment

### 3.3 Main experiment- wake behind a wind turbine

A sketch of the experimental setup in the large tunnel can be seen in figure 14

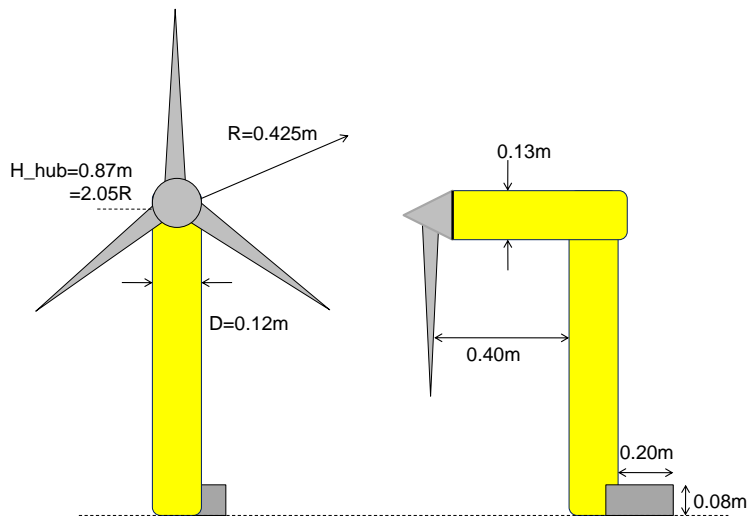


Figure 14: Wind tunnel set-up

#### 3.3.1 Tower wake

Wake measurements behind the wind turbine tower with the blades taken of will be done at  $x=4.5D$ ,  $x=8.5D$ ,  $x=14.55D$  and  $x=28.5D$  to compare with the cylinder wake from the reference experiment and the tower wake found in the wind turbine wake.

### 3.3.2 Turbine operation

At  $x=1.5D$ ,  $x=3.5D$ ,  $x=6.5D$ ,  $x=14.5D$  and  $x=28.5D$  will be done behind the model wind turbine for low, optimum and high TSR. The profile of the turbine blades is not known. To find desired operation conditions, the performance curves for the wind tunnel will be found by logging torque, thrust and reference wind speed for a range of rotational speeds. The rotational speed was controlled by a Micromaster 440 and varied according to expected wind speed to get measurements at the whole range of tip-speed ratios. Photos of the model wind turbine are showed in figure 15. During the experiment the cables from the torque meter and the optic photocell in the nacelle were taped to the back of the tower to minimize influence on the flow. Direction of rotation is clockwise.

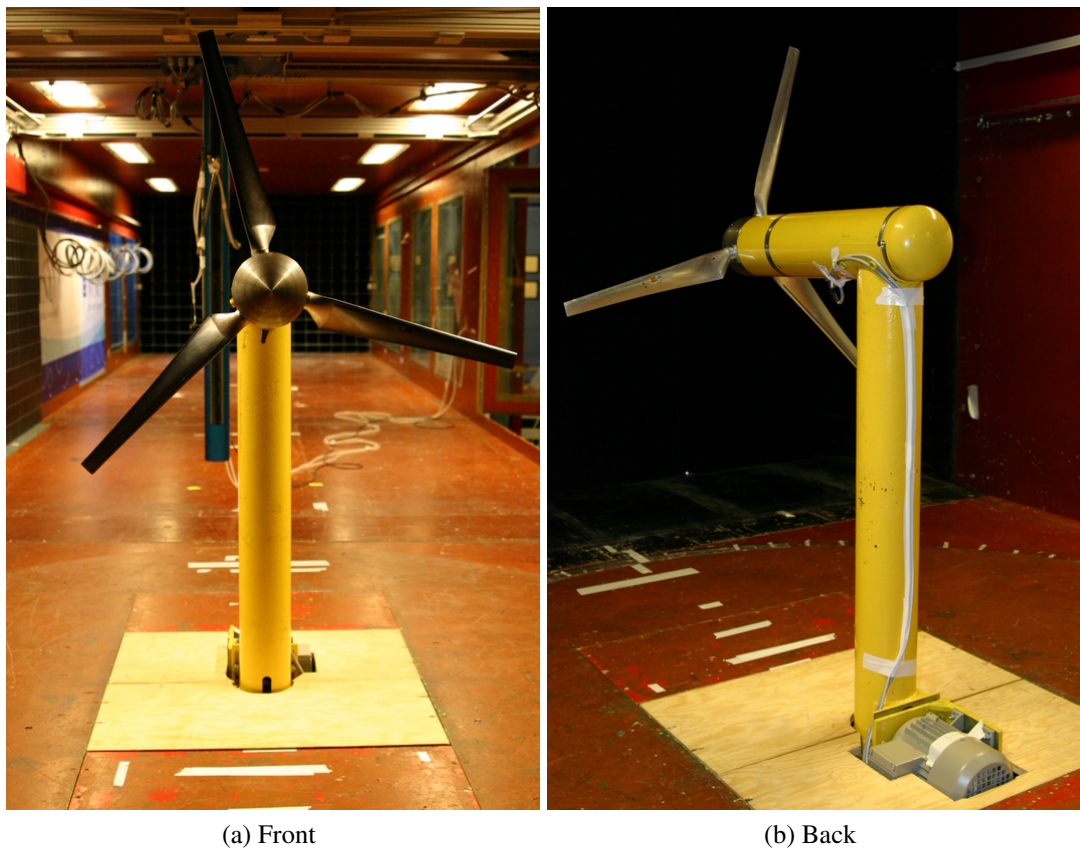


Figure 15: The model wind turbine

### 3.3.3 Grid size

To map the wake correctly the measurement grid must be sized so that the information wanted can be gathered with highest possible accuracy. It is important to find the maxi-

imum velocity deflection behind the tower, the width of the tower wake and to have one data point that is outside the total wake of the turbine. A higher density of data points is needed in the region behind the center of the tower and at the expected boundaries of the wake. Since the wake is expected to rotate (see section 2.3.2.1) the point of maximum velocity deflection will shift in the opposite direction of the blade rotation as the wake propagates downstream. This calls for a shift in the high density of measurement points to catch the wake center and edges.

### 3.3.4 Wind speed

When the wind turbine is running, it will affect the wind speed in the tunnel. To find the exact operating speed a reference velocity will have to be used. By using the pressure difference between before and after the contraction of the wind tunnel. Using Bernoulli's equation (88) and the area relation (89), assuming incompressible fluid, the wind speed  $U_{contr}$  at the inlet of the tunnel can be found with equation (90).

$$p_1 + \frac{1}{2}\rho U_1^2 = p_2 + \frac{1}{2}\rho U_2^2 \quad (88)$$

$$U_1 A_1 = U_2 A_2 \quad (89)$$

$$U_{contr} = \sqrt{\frac{2\Delta p_{contr}}{\rho(1 - \frac{A_2^2}{A_1^2})}} \quad (90)$$

$$\frac{U_{hub}}{U_{contr}} = \sqrt{\frac{\Delta p_{pithub}}{\Delta p_{contr}}(1 - \frac{A_2^2}{A_1^2})} \quad (91)$$

### 3.3.5 Blockage and scaling effects

Rotor diameter of the model wind turbine is 0.85m, a tower width of approximately 0.11m and hub height of 0.87m, give a total frontal area of  $0.5750m^2$ . Compared to the  $4.86 m^2$  area of the 2.7mx1.8m tunnel give a blockage ratio of 11.8%, which is in the high range of tolerated blockage ratio for wind tunnel experiments. 10% is considered as a higher limit to avoid wall interference on measurements. As long as the wake can expand freely this is not expected to be a major source of uncertainty [2]. Using

the WAsP wake model [2] at the furthest measuring point,  $x=4D_{rot}$ , the wake width is calculated to be around  $1.4D_{rot}$ , which is less than half the width of the tunnel  $\sim 3.2D_{rot}$ . Therefore, the wake expansion is not expected to be affected by the wind tunnel walls and wall effects are not corrected for in this study. For the reference experiment the cylinder diameter was 0.025m and the height of the test section 0.46m. This gives a blockage ratio of 5.4% which is found to have an insignificant effect on wind tunnel measurements [21].

With a scaling of 1:100 the nacelle length and tower width be approximately 50m and 11m, respectively. A wind turbine with rotor diameter and tower height around 90m will have a tower width around 4m and 2m at base and top respectively, so it is assumed that the tower wake observed in this experiment will be less prominent for a real turbine. The long distance from tower to the rotor plane on the model turbine will reduce the tower shadow or tower dam effect on the rotor blades, but this will not affect the tower wake particularly.

### 3.3.6 Similarity criteria

To make sure that the simulated boundary layer is comparable to the atmospheric boundary layer some similarity criteria must be fulfilled.

Because of the small scale of the model turbine compared to reality it is difficult to obtain the same Reynolds number in the experiment. Strips of roughness are placed at 10% of the cord length on the blades to make the transition from laminar to turbulent boundary layer happen faster, but some model effects are expected. Low Re will cause lower  $l/d$  ratio, especially in the case with lower turbulence level [9]. Since the TSR is adjusted by changing the rotational speed of the rotor and keeping the free stream velocity constant, the difference in Re seen by the blades (using chord length instead of D in equation (19)) will be quite large between lowest and highest TSR. Even if the Reynolds number is lower than in real life, the Re behind the rotor seen by the tower will be highly turbulent and the flow around the tower will have a lower critical Re and might be supercritical. Early transition to turbulent boundary layer and a narrower (and more intense if transcritical) wake is assumed to form compared to the reference wake studied at  $Re \sim 10^4$ .

The Rossby number gives the relationship between the local acceleration and the Coriolis acceleration. The Coriolis force is negligible unless for very large scales of motion

and will not cause any problem in the small scale experiment.

$$Ro = \frac{U}{L\Omega} \quad (92)$$

The Prandtl number is the ratio of heat dissipation to heat conduction. Since air is used in the wind tunnel as well as in nature the Prandtl number will be the same.

$$Pr = \frac{\nu}{\frac{k}{\rho}C_p} \quad (93)$$

The Eckert number is the ratio of kinetic energy to enthalpy, and is not of importance as long as the velocity is far below speed of sound.

$$Ec = \frac{U^2}{C_p\Delta T} \quad (94)$$

The Gross Richardson number is the ratio between inertial forces and gravitational forces, and is zero in a neutral ABL.

$$Ri = \frac{\Delta T}{T} \frac{L}{U^2} g \quad (95)$$

## 4 Results

### 4.1 Reference experiment behind cylinder in small wind tunnel

x	D[m]	$U[\frac{m}{s}]$	Re	$C_{d,exp}$	$\theta_{exp}$	$\Delta u_{max,exp}$	$y_{\frac{1}{2},exp}$	f [Hz]	St
4.5D	0.0242	10.35	16,700	0.641	0.0078	2.73	0.0140	89.72	0.210
8.5D	0.0242	10.35	16,700	0.675	0.0082	2.21	0.0199	89.72	0.210

x	D[m]	$U[\frac{m}{s}]$	Re	$C_{d,C_p}$	$\theta_{th}$	$\Delta u_{max,th}$	$y_{\frac{1}{2},th}$
4.5D	0.0242	10.35	16,700	1.077	0.013	6.16	0.0105
8.5D	0.0242	10.35	16,700	1.077	0.013	4.49	0.0145

Table 2: Summary of results (exp) and theory (th) from cylinder wake measurements

In figure 16 the variation of wind speed and TI in empty tunnel is plotted and shows very little variation and no interference from the wall boundary layers in the area of interest.

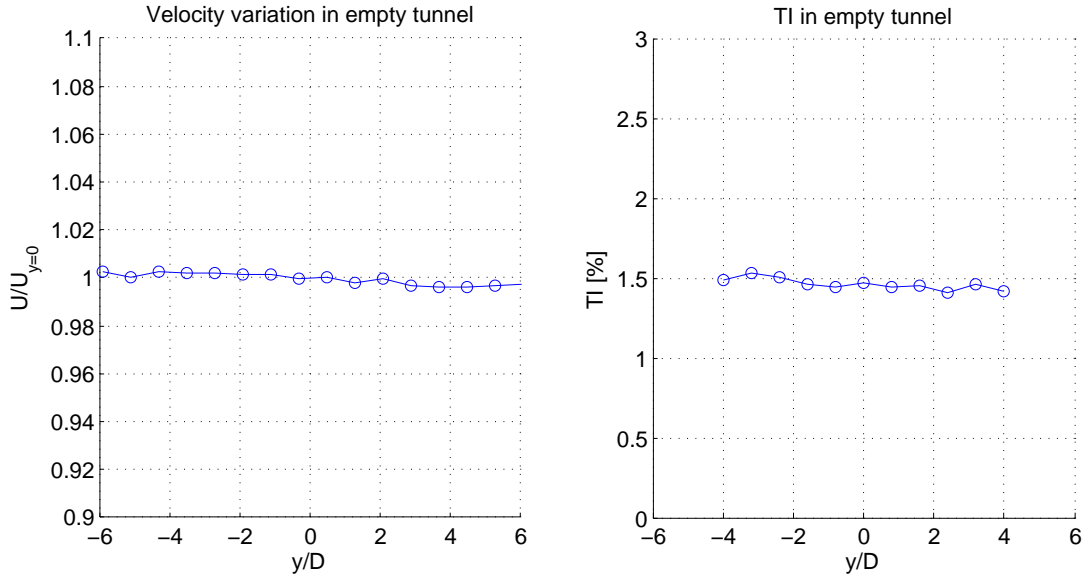


Figure 16: Wind speed and TI in empty tunnel

Pressure measurements done on the surface of the cylinder were done and are plotted against potential flow theory in figure 17.

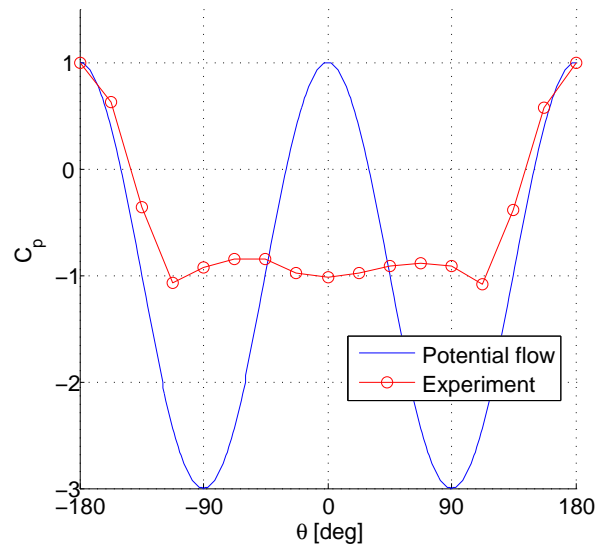


Figure 17:  $C_p$  on cylinder surface

Velocity and turbulence data were then gathered at  $x=4.5D$  and  $x=8.5D$  downstream of the cylinder. In figure 18 the velocity profiles are non-dimensionalised and plotted against classical wake theory. Turbulence intensity can be seen in figure 19.

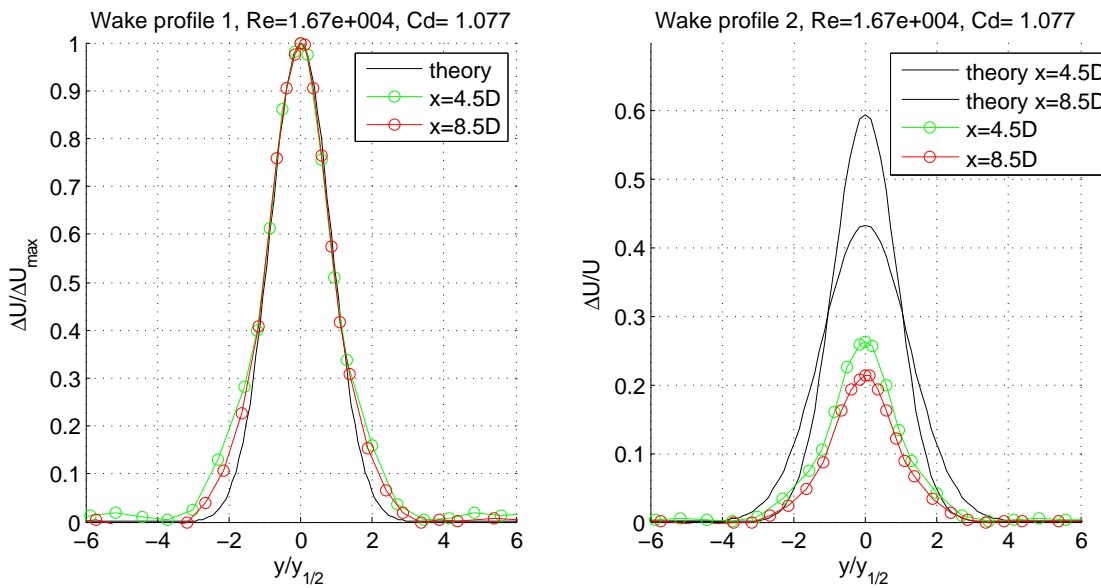


Figure 18: Non-dimensional velocity profiles in the wake



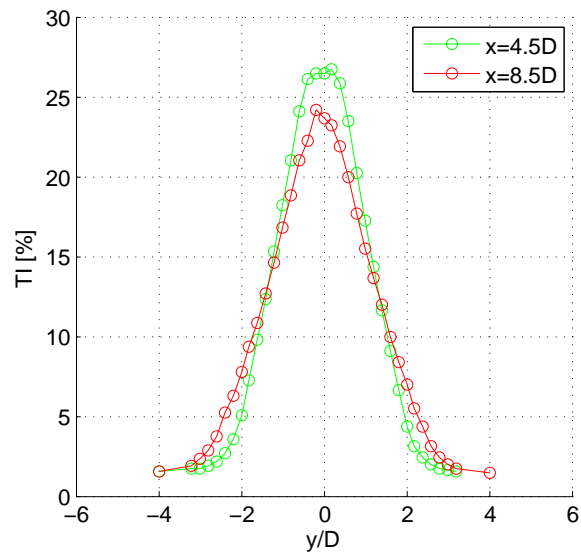


Figure 19: Turbulence intensity in wake

The power spectra for  $x=4.5D$  and  $x=8.5D$  downstream are shown in figure 20

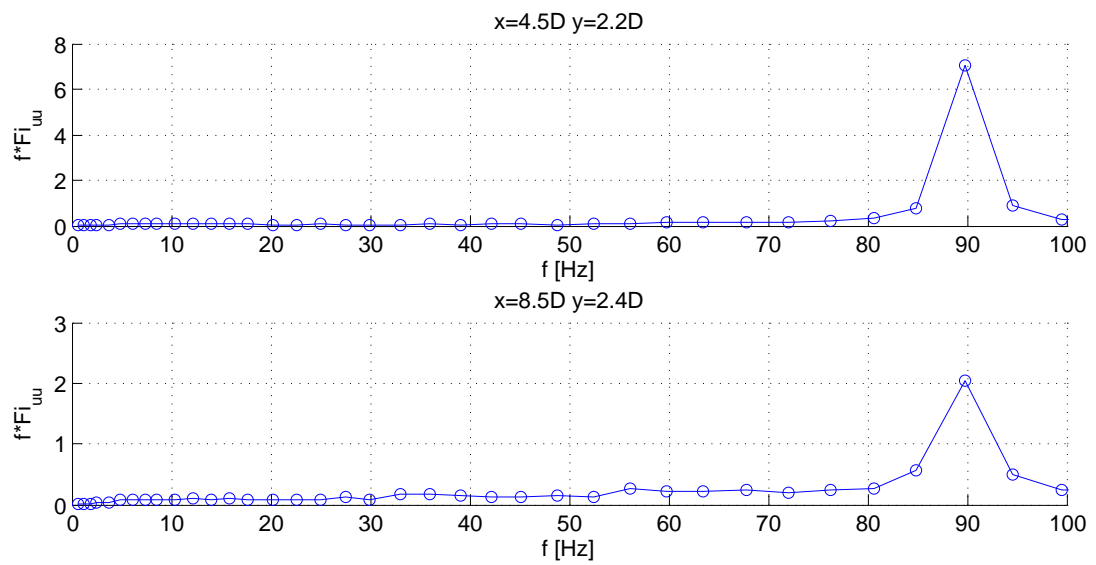


Figure 20: PSD for the cylinder wake

## 4.2 Large wind tunnel

For this experiment velocity and TI was not measured in empty tunnel, but from earlier studies done in the same wind tunnel the ground floor boundary layer was found to be 0.34m and the TI to be less than 0.2% outside this boundary layer [2, 3]. In this experiment the turbine is located further upstream, and the boundary layer is expected to be even thinner. The blade tips pass at  $z=0.445\text{m}$ , well outside the boundary layer in any case. In studies referred to above the velocity variation along the length of the test section was also found to vary negligible.

### 4.2.1 $C_p$ and $C_T$

Before doing measurements in the wake,  $C_p$  and  $C_T$  curves were found for the wind turbine. The wind tunnel was set to operate at a constant speed of  $9.64\frac{\text{m}}{\text{s}}$ , and thrust, torque and actual velocity found by the pressure drop over the contraction were logged for different rotational speeds of the turbine. With equations (77), (76) and (78) the curves for  $C_p$  and  $C_T$  were plotted as seen in figure 21. Highest efficiency was found at  $\text{TSR}=4.0$ , and half of maximum efficiency were found at  $\text{TSR}=3.0$  and  $\text{TSR}=6.25$ .

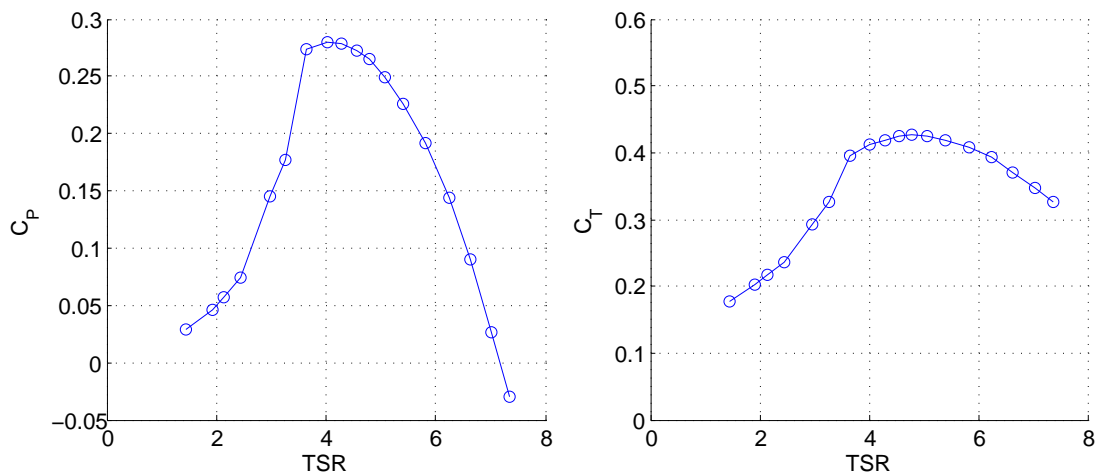


Figure 21:  $C_p$  and  $C_T$  curves

### 4.2.2 Tower wake

The rotor blades were taken off and the fan of the wind tunnel adjusted to obtain the same wind speed as when the wind turbine was operating. Measurements were taken at

$z=-R$  for  $x=4.5D$ ,  $x=8.5D$ ,  $x=14.5D$  and  $x=28.5D$ . A summary of the results from the tower wake measurements can be seen in table 3.

x	D[m]	$U[\frac{m}{s}]$	Re	$C_{d,exp}$	$\theta_{exp}$	$\Delta u_{max,exp}$	$y_{\frac{1}{2},exp}$	f [Hz]	St
4.5D	0.12	9.64	77,120	1.075	0.065	7.26	0.092	15.02	0.187
8.5D	0.12	9.64	77,120	1.306	0.078	3.17	0.155	13.55	0.169
14.5D	0.12	9.64	77,120	1.411	0.085	2.37	0.212	13.55	0.169
28.5D	0.12	9.64	77,120	1.553	0.093	1.59	0.330	13.55	0.169

x	D[m]	$U[\frac{m}{s}]$	Re	$C_{d,C_p}$	$\theta_{th}$	$\Delta u_{max,th}$	$y_{\frac{1}{2},th}$
4.5D	0.12	9.64	77,120	NA	0.048	5.03	0.043
8.5D	0.12	9.64	77,120	NA	0.048	3.66	0.061
14.5D	0.12	9.64	77,120	NA	0.048	2.80	0.080
28.5D	0.12	9.64	77,120	NA	0.048	2.00	0.111

Table 3: Summary of results (exp) and theory (th) from tower wake measurements

In figure 22 the wake profiles are compared with classical wake theory.

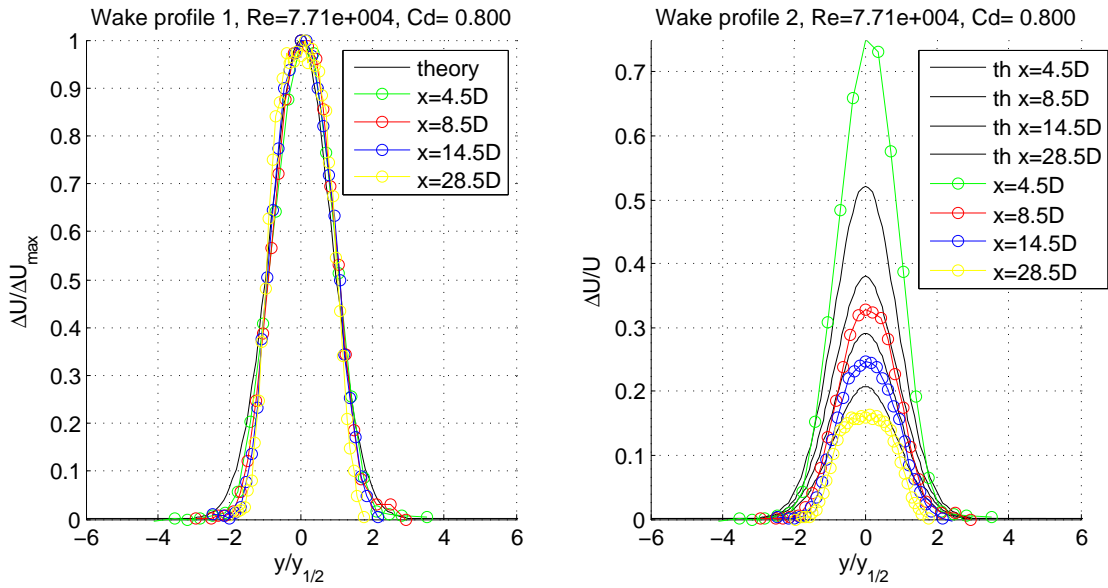


Figure 22: Non-dimensional velocity profiles in the tower wake

Turbulence intensity in the tower wake is shown in figure 23.

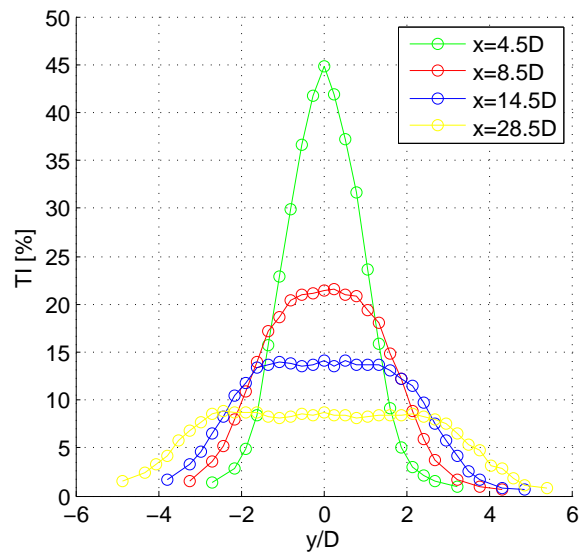


Figure 23: Turbulence intensities in tower wake

Vertical velocity profiles at the wake centers were also taken, to see if and how much the air flowing over the nacelle affected the horizontal wake profiles taken at  $z=-R$ . Results are shown in figure 24.

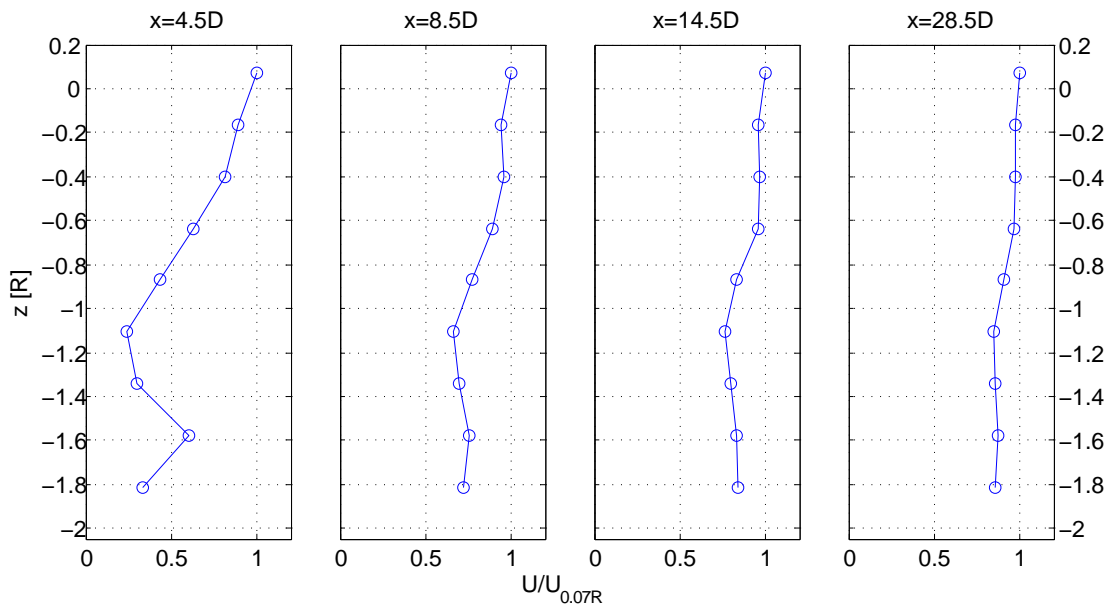


Figure 24: Vertical velocity profiles at wake center

Figure 25 show the measured growth rates for the tower wake.

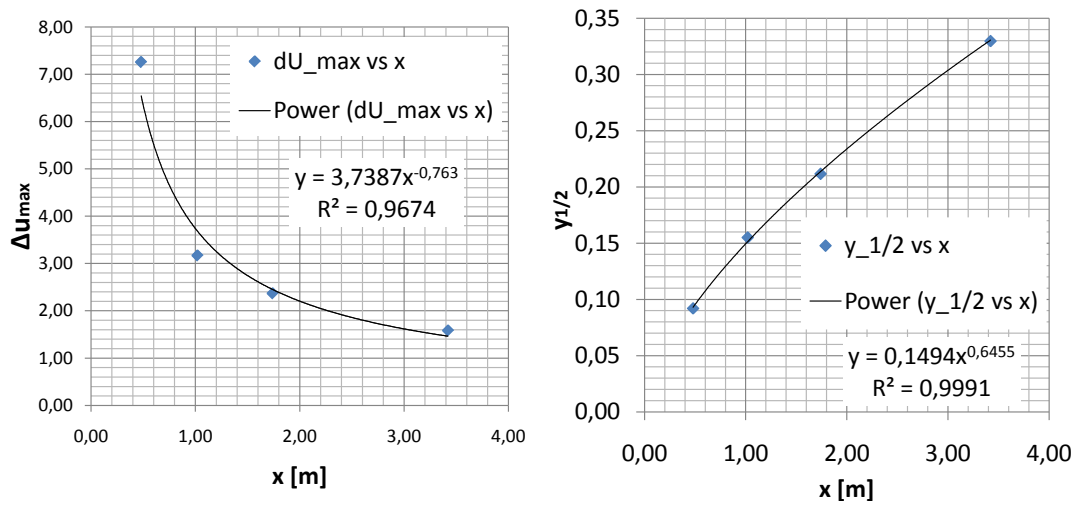


Figure 25: Measured growth rates for  $y_{1/2}$  and  $\Delta u_{max}$

Psd-plots for the tower wake is shown for the  $x=4.5D$ ,  $x=8.5D$ ,  $x=14.5D$  and  $x=28.5D$  in figure 26.

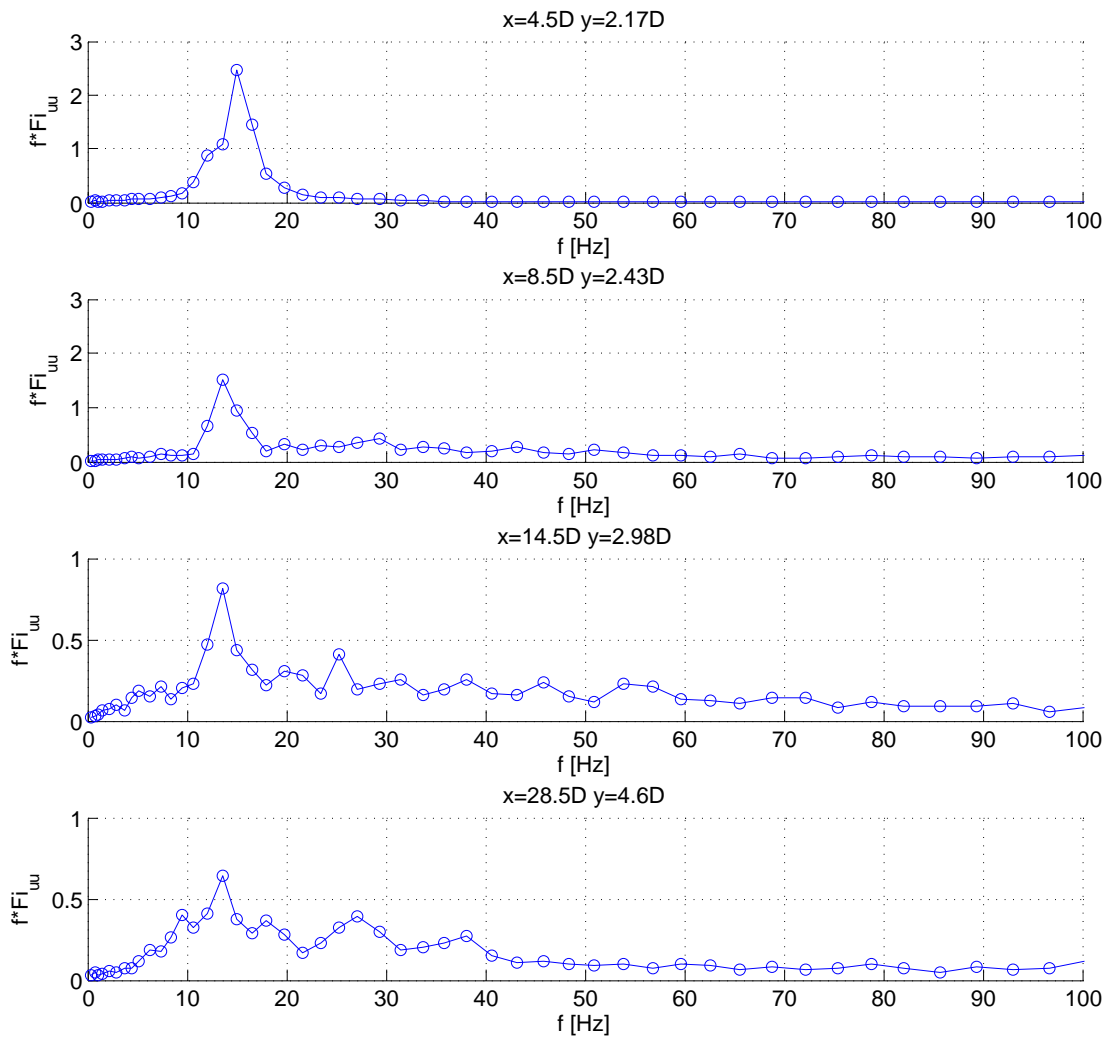


Figure 26: PSD for the tower wake

### 4.2.3 Wind turbine wake

An overview of the operating conditions for the wind turbine can be found in 4, and a summary of the results obtained can be seen in table 5.  $f_1$ ,  $f_2$  and  $f_3$  are the frequency where more or less distinct peaks in the PSD plots in figures 36- 37 were found.  $f_1$  show the vortex shedding frequency from the tower,  $f_2$  show the passing of the blades, and  $f_3$  the tip vortex frequency (if found).

TSR	$D_R$ [m]	$U$ [ $\frac{m}{s}$ ]	Re	RMP	3P [Hz]	$C_P$	$C_T$
3.00	0.85	9.65	781,190	644	32.2	0.145	0.465
4.00	0.85	9.62	778,762	868	43.3	0.280	0.586
6.25	0.85	9.64	780,381	1352	67.6	0.144	0.567

Table 4: Wind turbine operating conditions

TSR	x	$U$ [ $\frac{m}{s}$ ]	D [m]	f1 [Hz]	f2 [Hz]	f3 [Hz]	St (from f1)
3.00	3.5D	9.64	0.12	16.85	32.96		0.210
	6.5D	9.64	0.12	16.85	32.96		0.210
	14.5D	9.64	0.12	14.65	32.96		0.182
	28.5D	9.64	0.12	14.65	32.96		0.182
4.00	3.5D	9.64	0.12	14.65	43.21	30.03	0.182
	6.5D	9.64	0.12	14.65	43.21	30.03	0.182
	14.5D	9.64	0.12	14.65	43.21	30.03	0.182
	28.5D	9.64	0.12	14.65	43.21	30.03	0.182
6.25	3.5D	9.64	0.12	14.65	67.39		0.182
	6.5D	9.64	0.12	14.65	67.39	54.20	0.182
	14.5D	9.64	0.12	14.65	67.39	54.20	0.182
	28.5D	9.64	0.12	14.65	71.78	51.54	0.182

Table 5: Summary of results from wind turbine wake measurements

For each of the three operating conditions a grid of both Pitot and hot wire measurements were taken at five locations downstream of the turbine. Measurements were taken at  $x=1.5D$ ,  $x=3.5D$ ,  $x=6.5D$ ,  $x=14.5D$  and  $x=28.5D$ , with  $D$  as the tower diameter of 0.12m, and  $x_0$  as center of the tower. To start with six horizontal measurements series were taken between  $z=-0.30R$  and  $z=-1.35R$ ,  $R$  being the rotor radius of 0.425m and  $z_0$  the rotor center. As the experiment proceeded this was changed to four series due to lack of time. Between 18 and 33 points were taken at each horizontal measurement series with higher density around the expected wake center. The outermost data points were chosen depending on the distance downstream of the tower. In the figures below the data points are shown as black dots, together with the outline of the wind turbine. The figures show the wake from a viewing point upstream of the turbine.

At  $x=1.5D$  the Pitot measurements gave negative velocity behind the tower, and are not shown here. The TI measurements at  $x=1.5D$  are also omitted, but can be found in the appendix C.4. For the highest TSR no measurements were taken at  $x=1.5D$ .

#### 4.2.4 Comparison of wake profiles

In figures 27 and 28 the wake velocity profile at  $x=3.5D$ ,  $x=6.5D$ ,  $x=14.5D$  and  $x=28.5D$  for different TSRs are compared with the tower wake velocity profile.

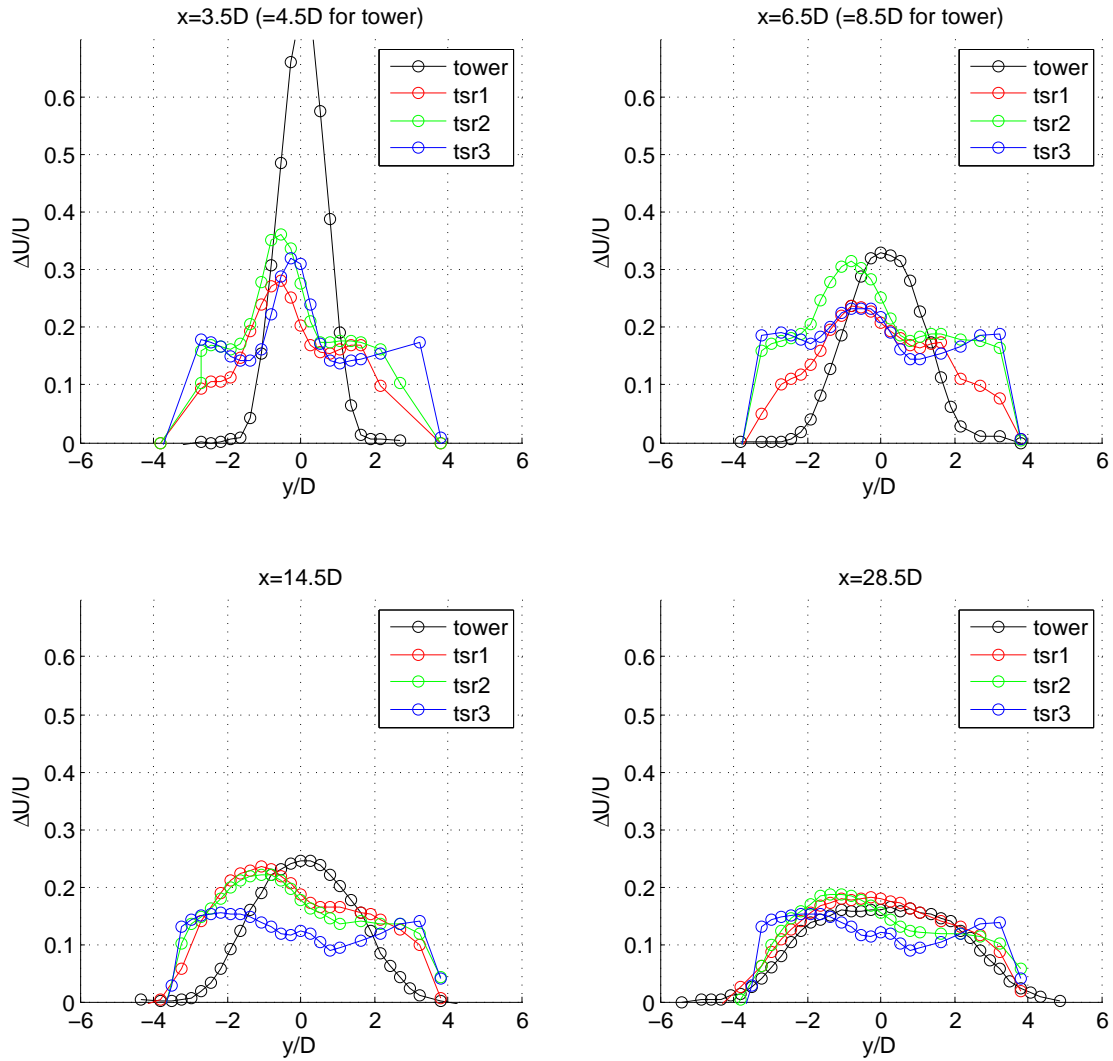


Figure 27: Wake velocity profiles at  $z = -0.3 R$



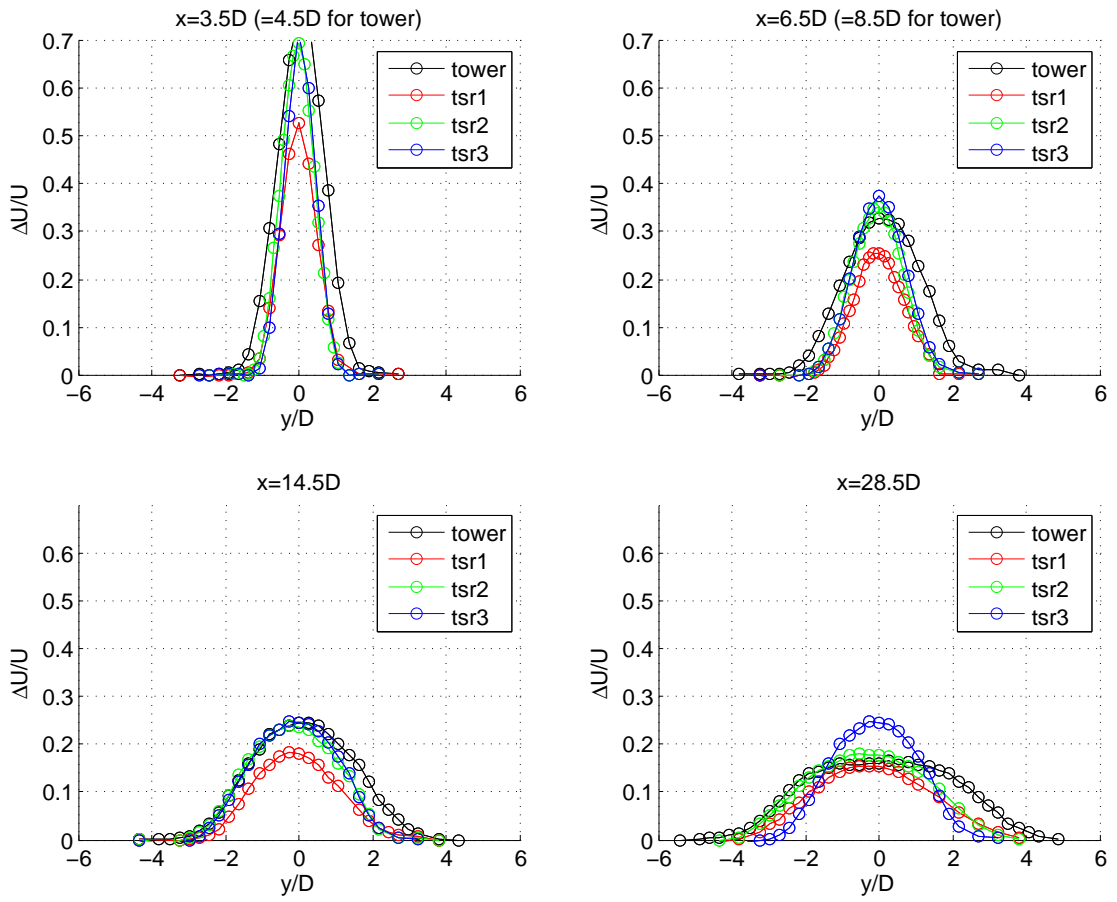


Figure 28: Wake velocity profiles at  $z = -R$

**4.2.4.1 Wake of turbine operating at optimum TSR** Figures 29 and 30 show streamwise velocity and streamwise TI in the wake of the turbine operating at TSR=4.0, respectively.

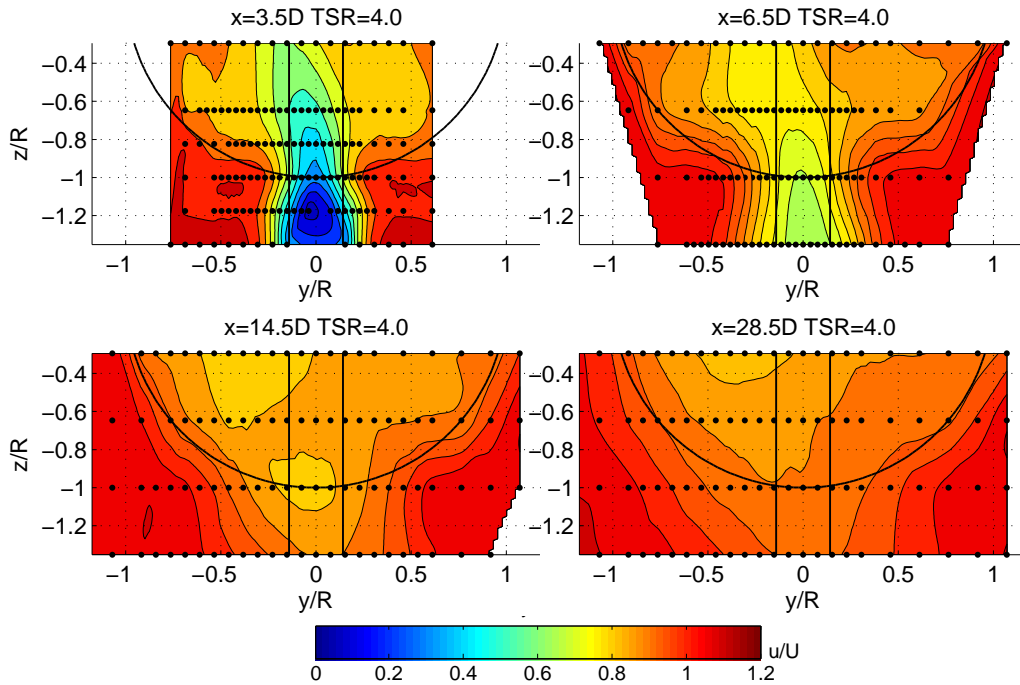


Figure 29: Streamwise velocity in the wake of the turbine operating at TSR=4.0

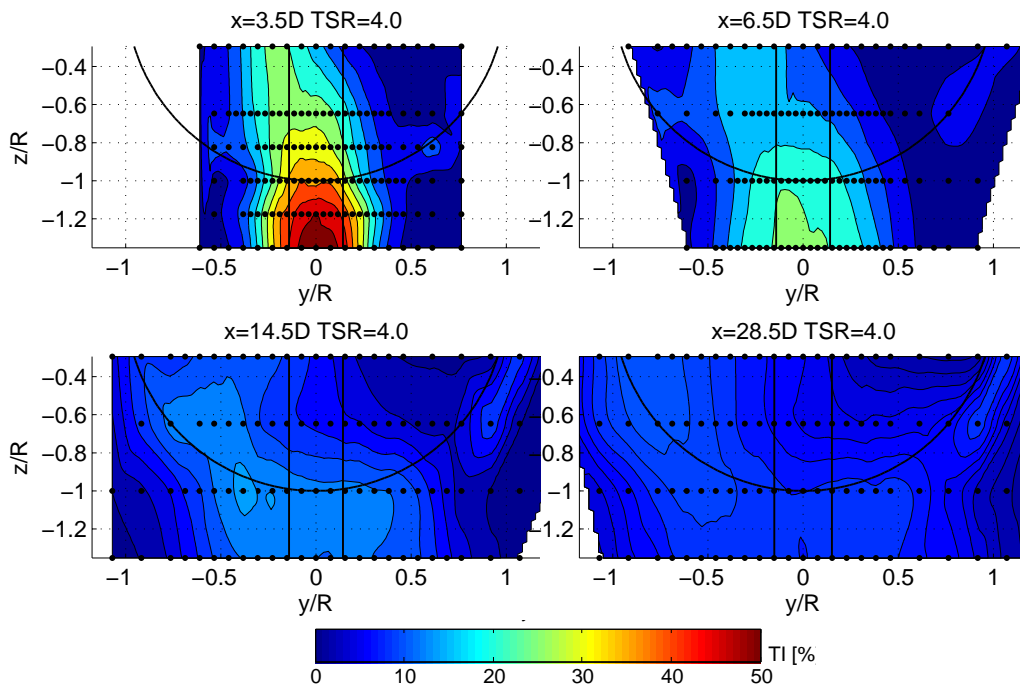


Figure 30: Streamwise TI in the wake of the turbine operating at TSR=4.0

**4.2.4.2 Wake of turbine operating at low TSR** Figures 31 and 32 show streamwise velocity and streamwise TI in the wake of the turbine operating at TSR=3.0, respectively.

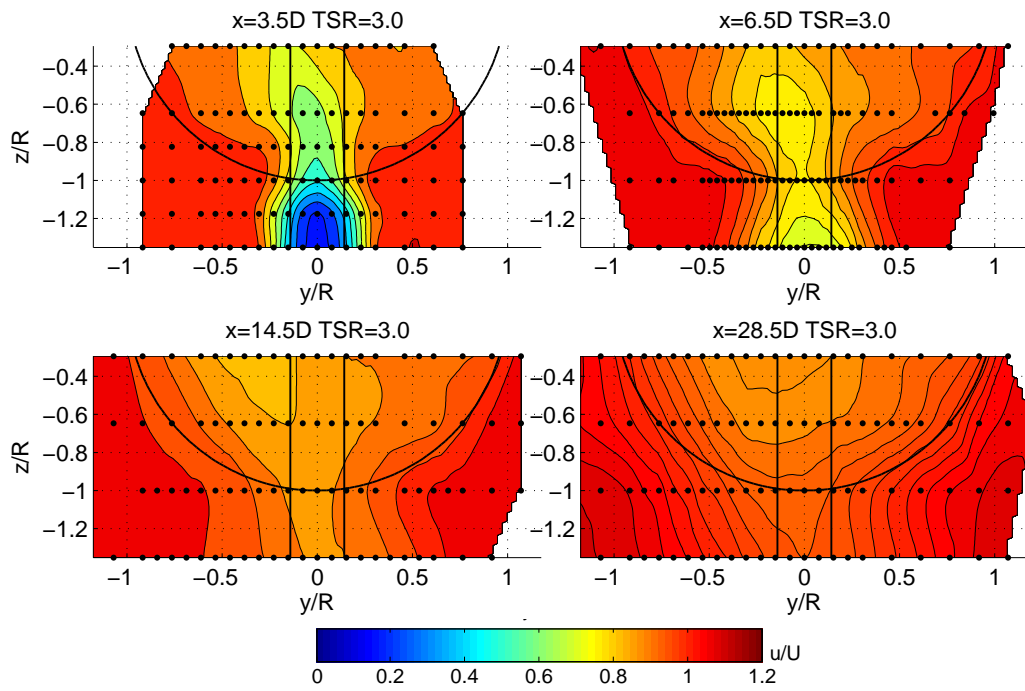


Figure 31: Streamwise velocity in the wake of the turbine operating at TSR=3.0

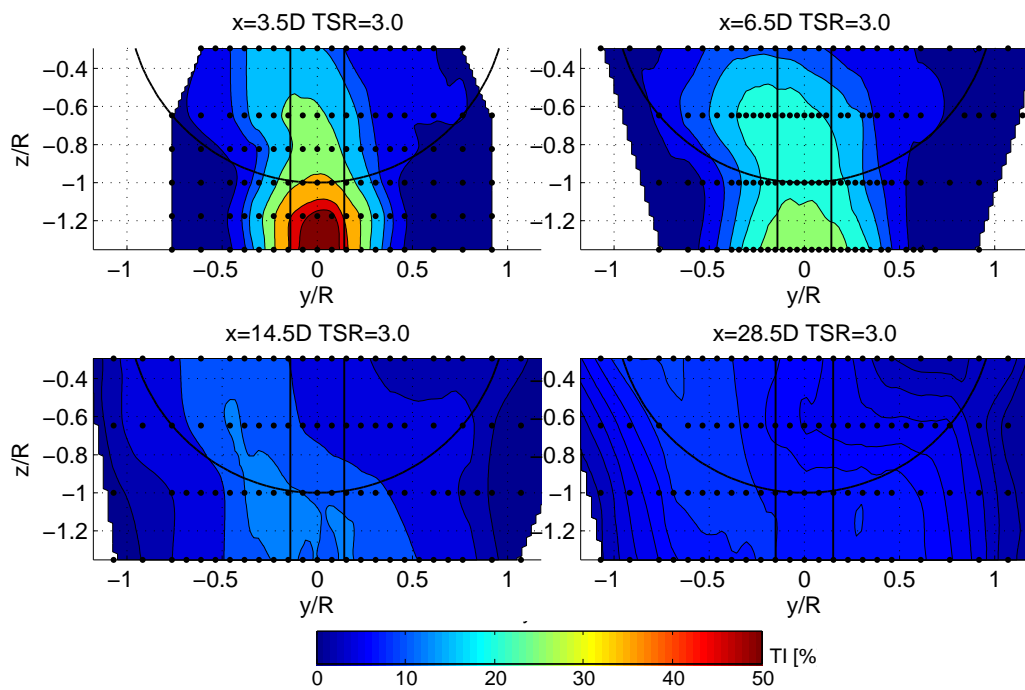


Figure 32: Streamwise TI in the wake of the turbine operating at TSR=3.0

**4.2.4.3 Wake of turbine operating at high TSR** Figures 33 and 34 show streamwise velocity and streamwise TI in the wake of the turbine operating at  $TSR=6.25$ , respectively.

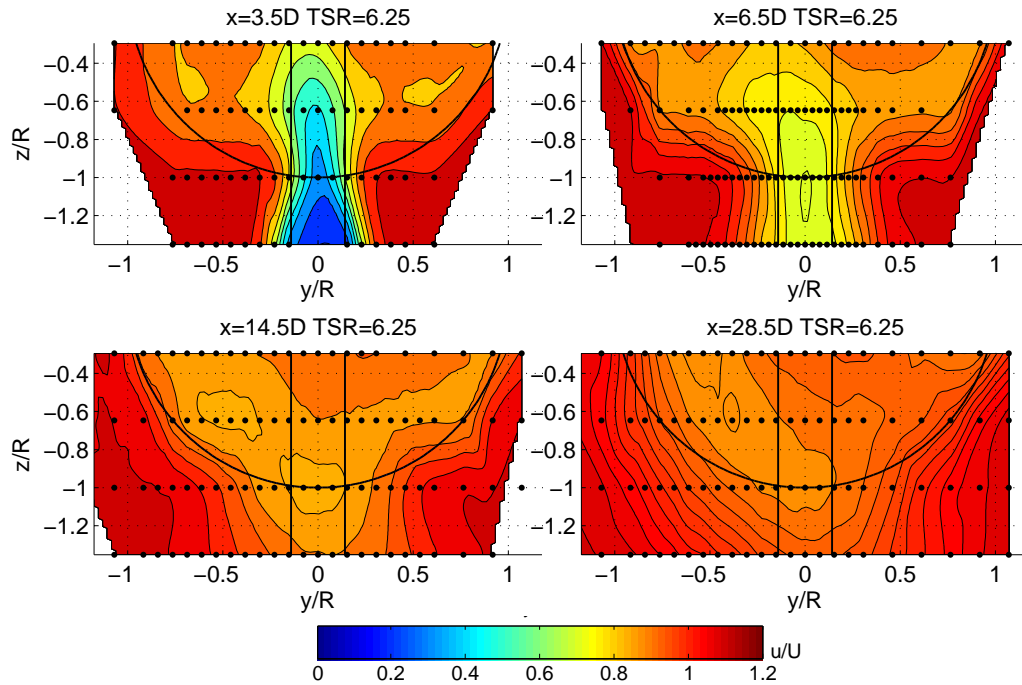


Figure 33: Streamwise velocity in wake of the turbine operating at  $TSR=6.25$

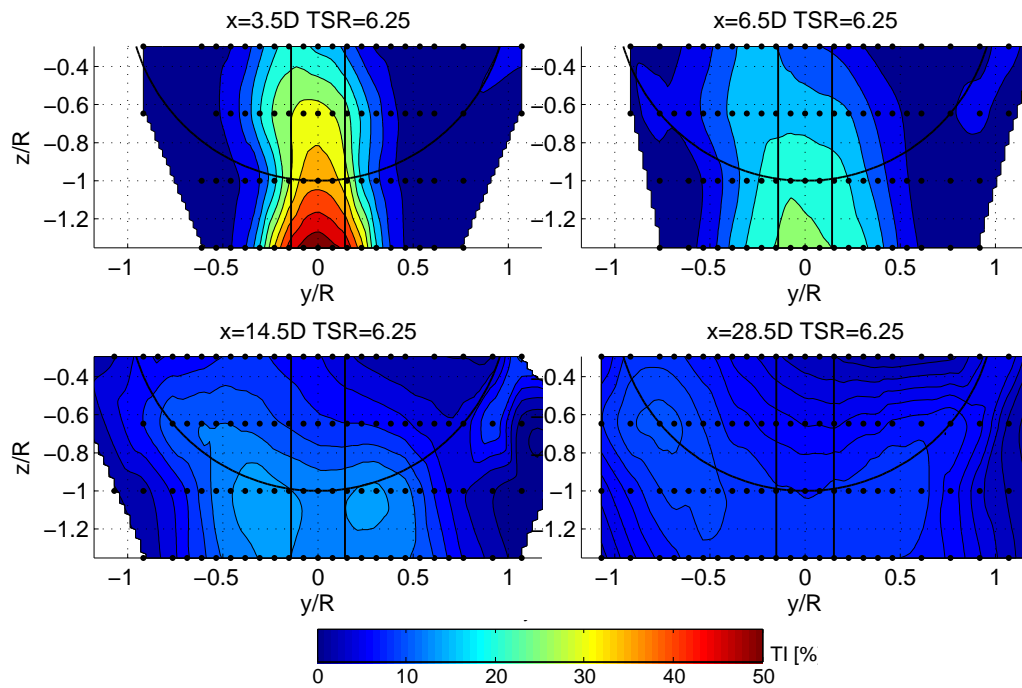


Figure 34: Streamwise TI in wake of the turbine operating at  $TSR=6.25$

**4.2.4.4 PSD in wind turbine wake** Figures 35, 36 and 37 shows the PSD at selected points with the turbine operating at optimum, low and hig TSR, respectively.

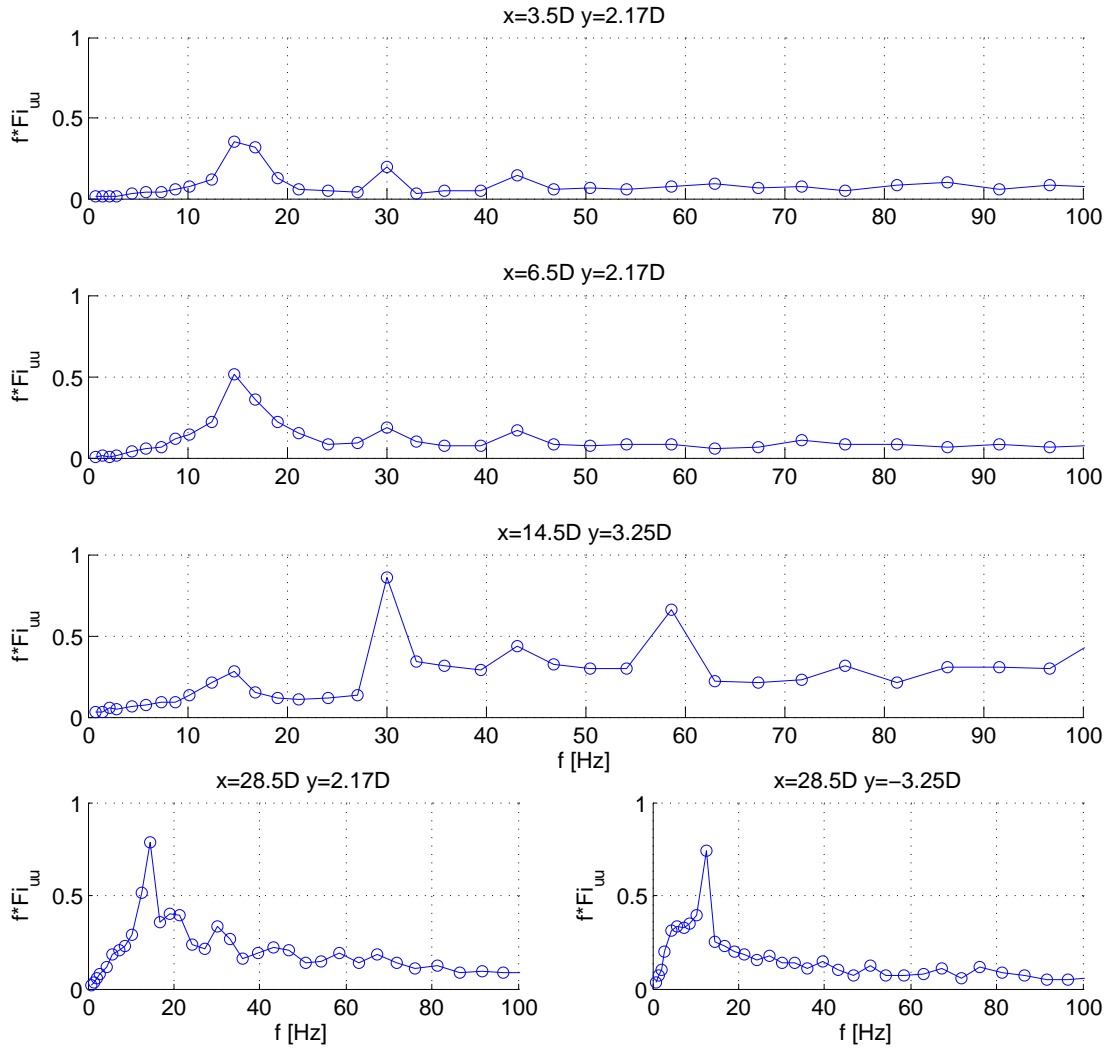


Figure 35: PSD for wind turbine wake operating at TSR=4.0

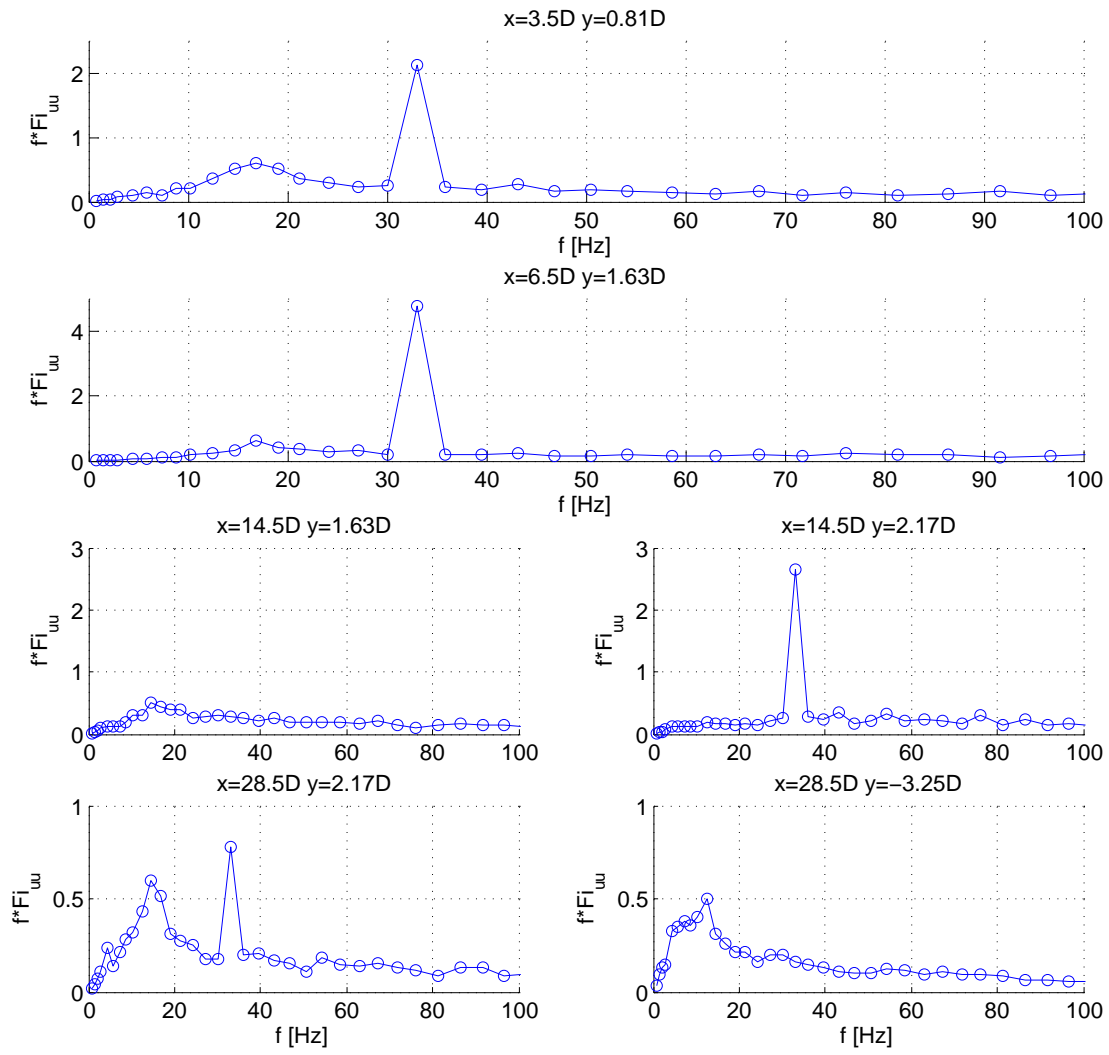


Figure 36: PSD for wind turbine wake operating at TSR=3.0

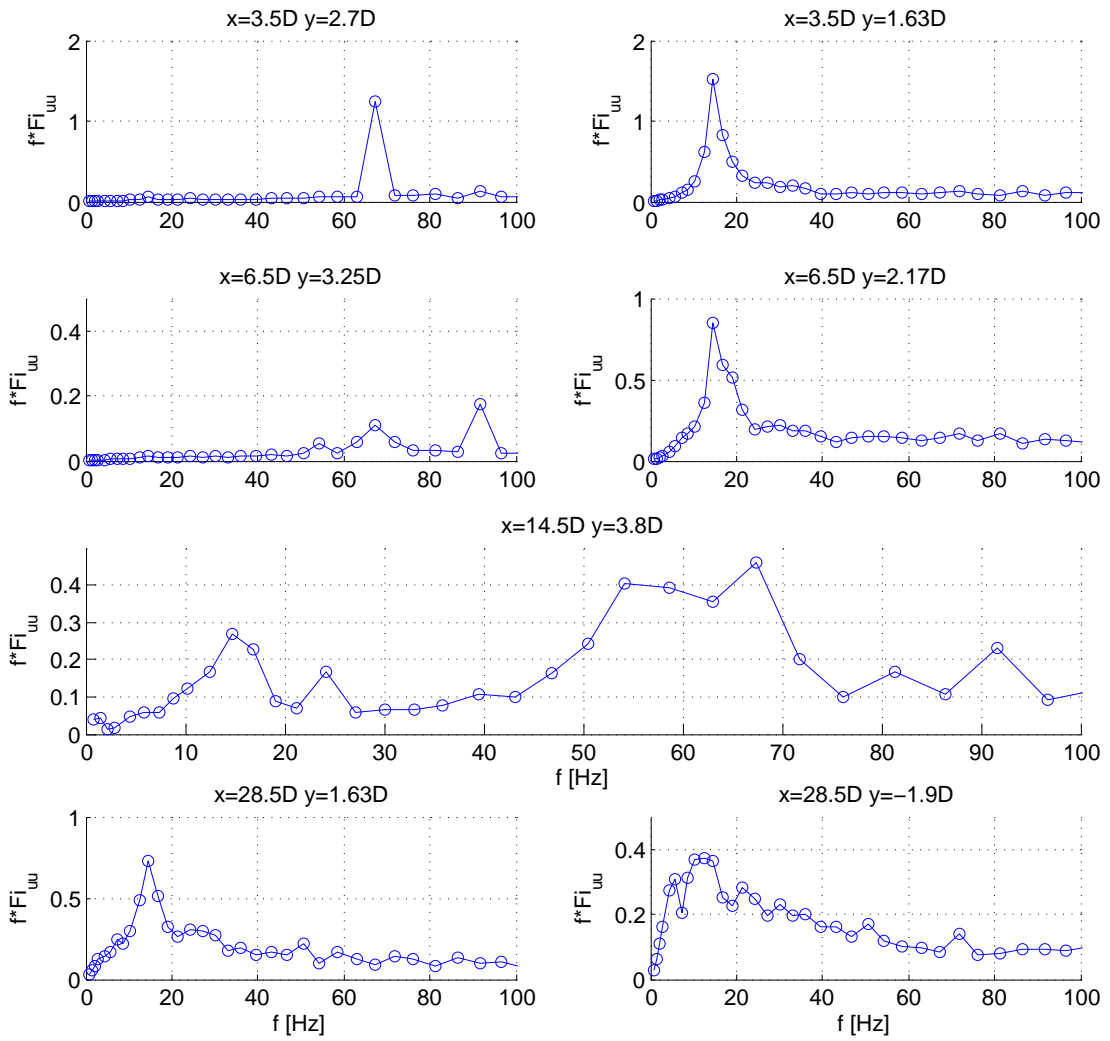


Figure 37: PSD for wind turbine wake operating at TSR=6.25

## 5 Discussion

### 5.1 Reference measurements behind cylinder in small wind tunnel

Empty tunnel measurements for velocity and TI were taken to see if wall boundary layers affected the area of interest. In figure 16 the wind speed variation in empty tunnel is plotted and it shows very little variation and no interference from the wall boundary layers in the area of interest. Streamwise TI in the same figure show a constant TI around 1.5%. Average wind speed were found to be  $10.35 \frac{m}{s}$ , which gives  $Re=16,700$  with cylinder diameter of 0.0242m and  $\nu = 1.5e - 5$ .

As seen in figure 17 the separation point is, as expected, on the windward side of the cylinder between 45 and 90 degrees from the stagnation point.

For the measured Reynolds number  $C_d$  of a smooth cylinder is expected to be between 1.0 and 1.2. In this experiment  $C_d = 1.0769$  was obtained from pressure measurements on the cylinder surface, which is as expected.

The non-dimensional velocity profile shown in "Wake profile 1" in figure 18 fits fairly well with the theoretical profile proposed by Wygnanski [27], but deviates at the edges of the wake. A deviation near the edges are expected because the theory use constant eddy viscosity, which does not hold at the edges where the flow changes between fully turbulent wake flow and irrotational free stream flow [23]. The theoretical profile is expected to give a wider wake, but here the experimental profile is wider.

"Wake profile 2" in figure 18 show the measured velocity defects at  $x=4.5D$  and  $x=8.5D$  together with the calculated velocity profile using the growth-rate expressions in equation (45). Here it becomes clear that the measured profile deviates quite a bit both in size and shape compared to the theoretical. The wake has a weaker and narrower peak and a more gradual approach to the free stream velocity than the theoretical wake.  $C_d = 1.077$  from the pressure measurements are used for calculating the theoretical profile. However, calculating  $C_d$  using the momentum equation and integrating across the measured profile, values obtained were only 0.641 and 0.675 for  $x=4.5D$  and  $x=8.5D$ , respectively. The experiment were done at fairly low  $Re=16,700$ , but according to figure 1,  $C_d$  should be around 1.2. Turbulence intensity in the free stream is only around 1.46% and the surface of the cylinder is smooth. Even if the TI and surface roughness were high it is not expected that the flow can become critical with  $Re$  this low. Wake measurements (not shown here) behind a larger cylinder at higher speed, obtaining  $Re \approx 44,000$ , were also



done but with the same results. Since the blockage ratio is only 5% it is not expected to influence the results significantly.

With PSD analysis using a Hamming style window of  $2^{15}$  samples length, and overlap of 50% the shedding frequency was found to be 89.72Hz both at  $x=4.5D$  and  $x=8.5D$ . This gives Strouhal number equal to 0.21, which fits well with theory shown in figure 5.

## 5.2 Large wind tunnel

### 5.2.1 $C_P$ and $C_T$

With the wind turbine operating at a range of different rotational speeds thrust and torque were logged together with actual speed found from the pressure drop over the contraction. The performance curves are plotted in figure 21, and an overview of the wind turbine operating conditions and results for optimum, low and high TRS are given in table 4. Highest  $C_P = 0.280$  was found at  $TSR=4.0$ , half of the maximum  $C_P$  ( $\approx 0.14$ ) were found at  $TSR=3.0$  and  $TSR=6.25$ . These operating conditions were used in the later wake surveys.  $C_T$  measurements were taken for the free standing tower alone, and subtracted from the  $C_T$  obtained from the operating turbine. Thrust measured on the tower alone is expected to be larger than the actual contribution because the flow is laminar and will give higher  $C_d$  than the highly turbulent flow the tower experience in the area behind the rotor. However, the  $C_T$  values are believed to be more accurate with the tower drag subtracted.

Up to around  $TSR=2.0$  the blades operate at high angle of attack, are fully stalled and produce very little lift. Between  $2 < TSR < 4$  the blades gradually move out of stall and both lift and drag on the blades increase. At  $TSR=4.0$  the angle of attack has decreased so much that the blades operate at ideal angle of attack and non stalled condition.  $C_P$  reaches its maximum because the lift to drag ratio is highest. There is a steep change in the  $C_T$  curve due to the sudden change in lift force when the flow goes from being stalled to being attached. As  $TSR$  increase further the angle of attack increase and the  $C_P$  decrease as the lift to drag ratio drop.  $C_T$  still increase to a maximum around  $TSR=5.0$  since the combined lift and drag force on the blades shift towards the streamwise direction with the increasing angle of attack. For  $TSR > 5.0$  an increasing part of the blade, starting from the root, will operate at negative angle of attack and act as a propeller. The rotor feeds energy into the wake center and both  $C_P$  and  $C_T$  drop.

## 5.2.2 Tower wake

The drag coefficient  $C_d$  calculated from the velocity deficit using equation (56) were found to be 1.075, 1.306, 1.411 and 1.553 for  $x=4.5D$ ,  $x=8.5D$ ,  $x=14.5D$  and  $x=28.5D$ . Expected drag coefficient for a free standing cylinder of similar aspect ratio is around 0.8 [25], which is significantly lower than the measurements.

Compared with the theoretical profile in "Wake profile 1" in figure 22 the shape of all the profiles fits well, and have more distinct edges than the theoretical profile as described in [23]. When looking at "Wake profile 2" in the same figure the wake half width seems to fit, but the measured maximum velocity deviates from theory. Table 3 show a summary of the measured and expected key variables in the tower wake. In figure 25 the measured growth rate for  $\Delta u_{max}$  and  $y_{\frac{1}{2}}$  are plotted and show  $\Delta u_{max} \propto x^{-0.763}$  and  $y_{\frac{1}{2}} \propto x^{0.6455}$ , this also give an indication that the growth rate of the half width is closer to the theoretical  $\propto x^{0.5}$  than the maximum velocity deficit which should be  $\propto x^{-0.5}$ .

As seen in figure 23, the turbulence at  $x=4.5D$  is significantly higher than further downstream, and the velocity measurements might be influenced by this and give a lower value. The increasing  $C_d$  as the wake propagates downstream might be ascribed to the increased blockage as the wake expands. Since  $C_d$  is calculated from the velocity difference between wake and free stream, an increased free stream velocity caused by blockage effect will give a higher  $C_d$ .

Since wind turbine tower is a finite cylinder the wake will, at some point downstream, be disturbed by the air flowing over the top. Wake flow from the nacelle itself will also form and interfere with the cylinder wake. Considering the vertical velocity profiles in figure 24 the velocity, especially at  $x=4.5D$ , varies quite a bit. Depending on the height where the velocity profile is taken,  $C_d$  calculated from the velocity deficit would give very different results. To avoid the ground floor boundary layer and the free stream over the nacelle to the greatest extent possible, the tower wake measurement were taken at  $z=-R$ . The high speed seen at  $x=4.5D$ ,  $z=-1.6R$  might be due to an acceleration effect as the air flow over the motor controlling the wind turbine (see figure 15b). At the points further downstream there is a shift in velocity around  $z=-0.4R$ ,  $z=-0.6$  and  $z=-0.8R$  for  $x=8.5D$ ,  $x=14.5D$  and  $x=28.5D$ , respectively. This is assumed to be the boundary layer between the tower wake and the free stream flow over the nacelle. The flat top of the velocity profile at  $x=28.5D$ , and the generally smaller velocity deficits at  $x=8.5D$  and  $x=14.5D$  compared with theory, might be due to air from the free stream mixing with the wake and increasing the speed in the center.

The spectrum was calculated using a Hamming style window of  $2^{12}$  samples length, and an overlap of 50%. PSD for the tower wakes are plotted in figure 26, and peaks were found at frequencies 15.08Hz, 13.55Hz, 13.55Hz, and 13.55 Hz for  $x=4.5D$ ,  $x=8.5D$ ,  $x=14.5D$  and  $x=28.5D$  respectively. Using  $U=9.6\frac{m}{s}$  and the tower diameter of 0.12m gives Strouhal numbers 0.189 and 0.169 which is at most 15% below the expected  $St=0.20$ . Considering the uncertainty in the experiment this result is within the expected range.

### 5.2.3 Wind turbine wake

A summary of the results from the measurements done in the wind turbine wake can be seen in table 5. As said earlier the Pitot measurements at  $x=1.5D$  gave negative velocity behind the tower, and are not shown here. This close to the tower the flow is highly turbulent with considerable velocity gradients in  $y$  and  $z$  direction. There will also be a pressure gradient across the wake, and the lower static pressure will cause the Pitot to measure a too low velocity. Below the rotor plane (possibly in the ground floor boundary layer) some of the measurements taken at  $x=3.5D$  also gave negative velocity, but the results are shown to get a better picture of the wake development.

For the highest TSR no measurements were taken at  $x=1.5D$ . The TI plots from  $x=1.5D$  for the other TSR can be found in the appendix C.4

### 5.2.4 Comparison of velocity deficit in the wake profiles

Figures 27 and 28 compares the wake velocity profiles at  $z=-0.3R$  and  $z=-R$  for all the downstream distances for different TSR with the tower wake profiles. The peaks in the turbine wakes represent the influence of the tower. Generally these are narrower than the wake of the free standing tower. This can especially be seen at  $z=-R$ , where there is no trace of the rotor wake except the slight rotation to the left and the increased velocity deficit at higher TSR with higher  $C_T$ . The figure shows narrower and weaker tower wakes which probably is caused by the increased turbulence in the flow seen by the tower, producing a turbulent boundary layer and preventing the flow from separation to a point further back on the tower. This cause a narrower wake and the drag coefficient is reduced significantly according to theory.

The profiles at  $z=-0.3R$  show that the higher  $C_T$  in the cases with  $TSR=4.0$  and  $TSR=6.25$  give a stronger velocity deficit at  $x=3.5D$  than with  $TSR=3.0$ . The contour plots of

streamwise wake velocity (figure 33) for the turbine operating at  $TSR=6.25$  show that the expected velocity increase behind the wake center has not reached the height where the measurements are taken at  $x=3.5D$ . As the wake expands the area of higher velocity reach  $z=-0.3R$  at  $x=6.5D$ , and moves further outwards from the rotor center at measurements taken at  $x=14.5D$  and  $x=28.5D$ . For increasing  $TSR$  and increasing distance downstream the tower wake become less evident, and at  $x=28.5D$  the maximum wake velocity deficit is almost the same for all  $TSR$ . The profile for the lowest  $TSR$  looks similar to the tower wake profile, and increasing  $TSR$  gives flatter top and more distinct edges. Rotation of the turbine wake can be seen as the peak velocity deficit lies to the left of the wake of free standing tower, with stronger displacement for the high torque case at  $TSR=4.0$  than the two others.

**5.2.4.1 Wake behind wind turbine operating at optimum TRS** At  $x=3.5D$  and  $x=6.5D$  one can clearly see the outline of the tower in the total wake, both in the velocity and TI plot. At  $x=14.5D$  the tower is not so prominent on the velocity plot, but can be seen on the TI plot, the same goes for  $x=28.5D$ . The wake mix and form a more uniform profile and rounder shape as it moves further away from the turbine. As the wake propagates downstream the tower wake is displaced due to the clockwise rotation of the wake. This can be seen at all downstream points for both velocity and TI plots. At  $x=28.5D$  the remains of the tower wake can be seen on the left side of the TI plot at the edge of the rotor plane.

Tip vortices can be seen as a line with increased TI close to the blade tips at all downstream distances.

**5.2.4.2 Wake behind wind turbine operating at low TSR** Figures 31 and 32 show a more prominent tower wake at all distances downstream compared to the optimum  $TSR$  case. The total wake is smaller and weaker, and expands less as it propagates downstream. This is due the lower thrust experienced and the fact that the lower solidity by the slower rotating rotor means it can be modeled as a disc with smaller effective diameter than for a faster rotating rotor [16]. A weaker rotor wake will lead to less mixing and it takes longer time for the tower wake to disappear. Velocity and TI in the wake is not as uniform as it was behind the turbine operating at optimum  $TSR$ . Wake rotation is also smaller compared with the wake at optimum  $TSR$ , which is an expected result due to the lower torque on the blades. No tip vortices show on the TI plots.

**5.2.4.3 Wake behind wind turbine operating at high TRS** As for with lower TSR the wake behind a wind turbine operating at high TSR is expected to rotate less due to the lower torque on the blades. This can be seen in both figure 33 and 34. The velocity deficit and width of the rotor wake is also expected to be higher than for the turbine operating at lower TSR. Since the rotor can be regarded as a disc with solidity and diameter increasing with TSR, it will give a broader and stronger wake at higher TSR [16].

Behind the center of the rotor the wake velocity is higher than at the outskirts. As discussed earlier the inner part of the rotor blades act as a propeller due to the negative angle of attack and feeds energy into the wake flow. The air propelled into the center of the wake has lower turbulence intensity than the surrounding wake flow, and replace the turbulent air as the wake expands. This and the higher initial mixing cause the trace of the tower wake to die out quicker than for the cases with lower TSR, and both velocity and TI is more uniform across the rotor area. Tip vortices can be seen at  $x=6.5D$  and  $x=14.5D$ , but with the heavy mixing they are expected to die out quicker than for lower TSR.

**5.2.4.4 PSD analysis** In spectrum analysis a Hamming style window of  $10^{12}$  samples and overlap of 50% were used. PDS plots from  $z=-0.65R$  for the different TSR are shown in figure 36- 37, and key results listed in table 5. The height  $z=-0.65R$  were chosen to be able to capture both the rotor wake and tower wake with least interference from the nacelle. The points showed here were chosen to give the best representation of the characteristics of the spectrum in the wake without showing PSD plots for all points at all locations. Generally there were less distinct peaks in the center of the wake, and at  $x=28.5D$  signals were weaker and trace of both the vortex shedding frequency from the tower and the rotational frequency were hard to separate from the noise. This is expected because of the mixing and uniformity obtained this far downstream.

Peaks found at 16.85 and 14.65 are assumed to be the vortex shedding frequency from the tower and are slightly higher than the frequencies found in the wake of the free standing tower. This gives  $St=0.21$  and  $St=0.182$  using the velocity at hub height, and is within the expected range. Because of the axial induction factor it is believed that the actual speed seen by the tower can be as low as 70% of the speed at hub height. Over the rather long distance between the rotor plane and tower the air velocity might increase due to mixing with the free stream flow below the rotor, and is supposed to be higher than the induction factor suggests. In any case, the calculation of the Strouhal

number using a more accurate(lower) wind speed would give a higher value than what is given in table 5.

A peak were found at  $f_2=32.96\text{Hz}$  at  $\text{TSR}=3.0$ ,  $f_2=43.21\text{Hz}$  at  $\text{TSR}=4.0$  and  $f_2=54.20\text{Hz}$  at  $\text{TSR}=6.25$ . This is equal to three times the respective rotational frequency and represents the passing of the blades. For the turbine operating at optimum and high TSR a third peak were found at  $f_3=30.03\text{Hz}$  and  $f_3=54.20\text{Hz}$ , respectively. This is believed to origin from the tip vortices since the peaks were found to be stronger in the points where tip vortices can be seen in the wake plots, and does not exist for  $\text{TSR}=3.0$  where no such vortices could be seen. Studying tip vortices is outside the scope of this thesis, so this is not investigated further.

A disc normal to a stream is expected have a  $\text{St}=0.12$ . With the diameter of the rotor  $D_R=0.85\text{m}$  and free stream velocity  $U=9.64$  the expected peak would be at  $f=1.36\text{Hz}$  [16]. Due to the inferior number of samples and to low sampling frequency the expected peak representing the vortex shedding frequency from the rotor modeled as a disc of increasing diameter with TSR could not be found.

### 5.3 Uncertainty

There is always some uncertainty connected to experimental results. Several things can cause errors in the measurements compared to the actual values. Uncertainty is divided in three categories [19]:

- Spurious error
- Systematic error
- Random error

Spurious error is caused by human error or failure of measuring instruments. In this experiment the human error can be linked to the calibration of the pressure transducer using the fluid column manometer. The height of the column moved a little during the measurement. Another source of spurious error is alignment of the Pitot tube to the wind. The error is around 1% for  $5-10^\circ$ .

Systematic error is connected to the measuring instrument or the calibration of the measuring instrument. Poorly calibration, lack of linearity and hysteresis are usual sources for this kind of error. Some hysteresis was experienced in the fluid column manometer during calibration of the pressure transducer, and another calibration had to be done.

The numbers of calibration points were 7 for the transducers, 8 for the torque meter, 11 for the balance measuring thrust and 9 for the hot wire calibrations. The hot wire were calibrated every 1-2 hours to reduce the systematic error. (See A for calibration data.) The density of the fluid column manometer was not calibrated but expected to be constant for all measurements. For the torque calibration the angle of the rotor blade and hence the armlength used is a source of uncertainty. For the hot wire angle to the wind, and temperature variation may cause error. Error in rpm readings from the tachometer is expected to be small. The blade pitch was set to  $0^\circ$ , but a coarse scale for adjusting the angel may be a source of error. This is also expected to be low.

Random error comes from the measuring instrument giving different outputs at constant input, but can also be caused by small variations in the measured value due to variation in temperature and atmospheric pressure. In the experiment temperature was logged for each measurement point and atmospheric pressure taken at the start of each series. Increasing number of measurements reduces the random error. For the Pitot and hotwire measurements in the wake 900000 samples were taken at 3000Hz over 30 seconds. For torque, thrust and reference speed 7500 samples were taken at 500Hz over 15 seconds. Offset values were taken before each series. Random error is reduced by increasing the number of samples taken in a measurement. With 900000 samples over 30 seconds taken for velocity- and turbulence profile measurements, and 7500 samples over 15 seconds for reference speed, thrust and torque measurements the random error is also expected to be quite small.

The low Reynolds number in the reference experiment may be a cause of error. Using a higher wind speed and a larger cylinder would give a higher Re and flow conditions more suitable for comparison with the flow experienced by an anctual wind turbine tower.

## 6 Conclusion

To provide a basis for studying the influence of the tower on the total wake behind a wind turbine, measurements on a smooth cylinder were done. Drag coefficient, wake width and velocity deficit were studied and compared with theory. Drag coefficient was found by both pressure measurements on the cylinder surface and by calculating the momentum deficit in the wake. Pressure measurements gave a drag coefficient of 1.077, which is within the expected range, but when using the momentum deficit, drag coefficient was found to be of the order of 0.65. Several possibilities for this huge deviation from the expected theoretical drag coefficient of 1.2 have been discussed but without finding a satisfying explanation. The Strouhal number was found to be 0.21, as expected.

Wake studies behind the free standing wind turbine tower were also done finding a drag coefficient higher than expected. However, the shape and maximum velocity deficit matched theory fairly well accounting for influence from free stream flow over the top of the tower and blockage effects.

It has been found that the influence of the tower wake in the total wake of a wind turbine varies with the TSR. Compared to the wake of the free standing tower with the blades taken off, the tower wake in the wake of an operating wind turbine is narrower and weaker due to the high turbulence level in the stream seen by the tower. Strouhal number for the vortex shedding from the tower was found to be approximately the same in the wake of the free standing tower, the cylinder and in the total wake behind the operating wind turbine. For higher TSR the velocity deficit where higher, the tower wake less prominent and the turbulence and velocity profiles flatter across the width of the rotor. As expected, wake rotation and displacement of the tower wake in the wind turbine wake were found to be greater at optimum operating conditions of the wind turbine.



## **7 Further work**

For better accuracy of the reference measurements on the flow behind a circular cylinder, higher wind speed and TI would reproduce conditions closer to the flow experienced by the tower of a HAWT. To better match real operating conditions of a wind turbine a simulated boundary layer could be generated in the wind tunnel.

## References

- [1] NS-EN 1991-1-4. Eurokode 1: Laster på konstruksjoner - del 1-4: Allmenne laster - vindlaster, 2010.
- [2] M.S. Adaramola and P.Å. Krogstad. Experimental investigation of wake effects on wind turbine performance. *Renewable Energy*, 36(8):2078 – 2086, 2011.
- [3] M.S. Adaramola and P.Å. Krogstad. Performance and near wake measurements of a model horizontal axis wind turbine. under review, 2011.
- [4] S. Pal Arya. *Introduction to Micrometeorology*. Academic Press, 1988.
- [5] J.J. Bertin and R.M. Cummings. *Aerodynamics for Engineers*. Prentice Hall, 2008.
- [6] T. Bracchi. Dynamic loads on horizontal axis wind turbine. Master's thesis, Norwegian University of Science and Technology, 2009.
- [7] Nicholas J. Cook. The deaves and harris abl model applied to heterogeneous terrain. *Journal of Wind Engineering and Industrial Aerodynamics*, 66(3):197 – 214, 1997.
- [8] J. Counihan. Adiabatic atmospheric boundary layers: A review and analysis of data from the period 1880-1972. *Atmospheric Environment (1967)*, 9(10):871 – 905, 1975.
- [9] Ph. Devinant, T. Laverne, and J. Hureau. Experimental study of wind-turbine airfoil aerodynamics in high turbulence. *Journal of Wind Engineering and Industrial Aerodynamics*, 90(6):689 – 707, 2002.
- [10] Martin O. L. Hansen. *Aerodynamics of wind turbines*. Earthscan, 2<sup>nd</sup> edition, 2008.
- [11] Erich Hau. *Wind Turbines - Fundamentals, Technologies, Application, Economics*. Springer, 2<sup>nd</sup> edition, 2006.
- [12] C. G. Helmig, K. H. Papadopoulos, D. N. Asimakopoulos, P. G. Papageorgas, and A. T. Soilemes. An experimental study of the near-wake structure of a wind turbine operating over complex terrain. *Solar Energy*, 54(6):413 – 428, 1995.
- [13] J.F. Manwell, J.G. McGowan, and A.L. Rogers. *Wind Energy Explained*. Wiley, 2002.

- [14] M. E. McIntyre. Ib lecture notes on fluid dynamics. University of Cambridge's homepage, 2002.
- [15] D. Medici. Wind turbine wakes- control and vortex shedding. Technical report, KTH Mechanics, Royal Institute of Technology, 2004.
- [16] D. Medici and P.H. Alfredsson. Measurements on a wind turbine wake: 3d effects and bluff body vortex shedding. *Wind Energy*, 9:219–236, 2006.
- [17] D. Medici and P.H. Alfredsson. Measurements behind model wind turbines- further evidence of wake meandering. *Wind Energy*, 11:211–217, 2008.
- [18] K. H. Papadopoulos, C. G. Helmis, A. T. Soilemes, P. G. Papageorgas, and D. N. Asimakopoulos. Study of the turbulent characteristics of the near-wake field of a medium-sized wind turbine operating in high wind conditions. *Solar Energy*, 55(1):61 – 72, 1995.
- [19] Bjørn Winther Solemslie. Optimalisering av ringledning for peltonturbin. Master's thesis, Norwegian University of Science and Technology, 2010.
- [20] K. Son, J. Choi, WP. Jeon, and H. Choi. Effect of free-stream turbulence on the flow over a sphere. *Physics of fluids*, 22, 2010.
- [21] Stig Sund. The effect of blockage on high re flow over semi-circular obstacles. Master's thesis, Norwegian University of Science and Technology, 2010.
- [22] R. Szasz and L. Fuchs. Computations of the flow around a wind turbine: Grid sensitivity study and the influence of inlet conditions. In *Turbulence and Interactions*, volume 110 of *Notes on Numerical Fluid Mechanics and Multidisciplinary Design*, pages 345–352. Springer Berlin / Heidelberg, 2010.
- [23] H. Tennekes and J.L. Lumley. *A first course in turbulence*. The MIT press, 1972.
- [24] Matthias Türk and Stefan Emeis. The dependence of offshore turbulence intensity on wind speed. *Journal of Wind Engineering and Industrial Aerodynamics*, 98(8-9):466 – 471, 2010.
- [25] F.M. White. *Fluid Mechanics*. Mc Graw Hill, 2003.
- [26] F.M. White. *Viscous Fluid Flow*. Mc Graw Hill, 2006.
- [27] I. Wygnanski, F. Champagne, and B. Marasli. On the large-scale structures in two-dimensional, small-deficit, turbulent wakes. *Journal of Fluid Mechanics*, 168(-1):31–71, 1986.

- [28] F. Zahle, N.N. Sørensen, and H. Aagaard Madsen. Research in aeroelasticity efp-2007, chapter 3 - the influence of wind shear and tower presence on rotor and wake aerodynamics using cfd. Technical Report R-1649(EN), Risø  $\frac{1}{2}$  National Laboratory, Technical University of Denmark, 2007.

# A Calibration

## A.1 Calibration data

Transducer 1 calibration (traverse)

p	757,6 mmHG							
	101005 Pa							
g	9,82 m/s <sup>2</sup>							
R	287,05 J/KgK							
	h [m]	temp	rho	dyn pres	E	e	u	
	0		16,7	1,213982	0	-9,813	0	
	8	0,015	19,3	1,203189	23,568	-6,749	0,383	6,2590649
	13	0,0235	19,4	1,202778	36,9232	-5	0,601625	7,8355953
	18	0,033	19,5	1,202367	51,8496	-2,828	0,873125	9,2868675
	23	0,046	19,5	1,202367	72,2752	-0,325	1,186	10,96456
	28	0,064	19,4	1,202778	100,5568	3,592	1,675625	12,930879
	33	0,0875	19,3	1,203189	137,48	8,593	2,30075	15,117078
calibration con	60,316							

Transducer 2 calibration (contraction)

p	757 mmHG							
	100925 Pa							
g	9,82 m/s <sup>2</sup>							
R	287,05 J/KgK							
rpm	h [m]	temp	rho	dyn pres	E	e	u	
	0	0	19,7	1,200594	0	-8,967	0	
	100	0,0025	19,6	1,201004	3,928	-8,572	0,049375	2,5575758
	200	0,0105	19,6	1,201004	16,4976	-7,486	0,185125	5,2414707
	300	0,025	19,7	1,200594	39,28	-5,514	0,431625	8,0891461
	400	0,0435	19,9	1,199774	68,3472	-2,959	0,751	10,673959
	500	0,067	19,9	1,199774	105,2704	0,345	1,164	13,247024
	550	0,082	20,9	1,195694	128,8384	2,26	1,403375	14,680051
const	y = 91,534x - 0,3648							

HW calibration

temp	rho	pit E	hw E	hw e	pit u	hw u
18,5	1,202	-8,675	-9,343	0	0	0,001
18,7	1,201	-7,807	-0,856	8,487	0,212175	3,6601
19,3	1,199	-6,629	1,115	10,458	0,26145	5,6252
19,3	1,199	-5,589	2,141	11,484	0,2871	6,9085
19,3	1,199	-4,473	2,975	12,318	0,30795	8,0614
19,4	1,199	-3,217	3,703	13,046	0,32615	9,1892
19,4	1,199	-1,514	4,489	13,832	0,3458	10,5256
19,4	1,199	0,712	5,318	14,661	0,366525	12,051
19,4	1,199	3,386	6,154	15,497	0,387425	13,66
19,3	1,199	6,389	6,916	16,259	0,406475	15,2635
19,3	1,199	9,669	7,583	16,926	0,42315	16,8435

Figure 38: Data for calibration of transducers used for pitot measurements of reference and wake speed, and an example of the hw calibration

Thrust calibration

temp	E	kg	N	e	
24	-7,871		0	0	0
24	-6,258		0,95	9,329	0,268833
23,94	-5,415		1,45	14,239	0,409333
23,92	-4,608		1,95	19,149	0,543833
23,89	-3,765		2,45	24,059	0,684333
23,88	-2,912		2,95	28,969	0,8265
23,86	-2,086		3,45	33,879	0,964167
23,83	-1,244		3,95	38,789	1,1045
23,85	-0,404		4,45	43,699	1,2445
23,77	0,445		4,95	48,609	1,386
23,79	1,279		5,45	53,519	1,525

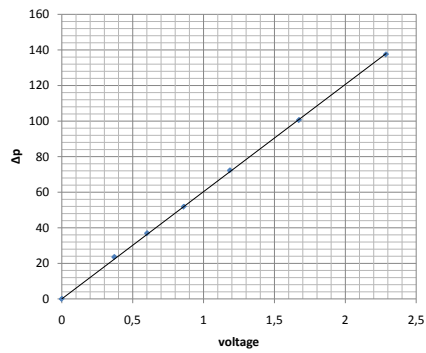
Torque calibration

arm 0,42 m

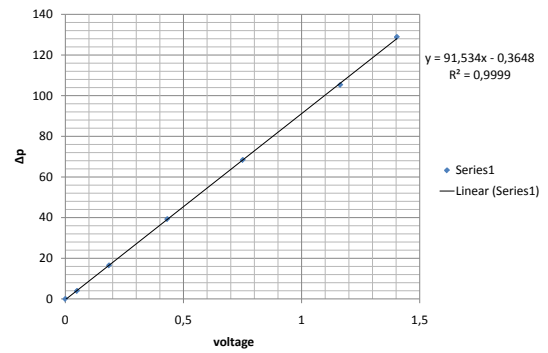
temp	E	kg	Nm	e	
24,56	8,472		0	0	0
24,51	7,434		0,066	0,27221	-0,519
24,42	6,615		0,116	0,47843	-0,9285
24,41	5,801		0,166	0,68465	-1,3355
24,36	4,989		0,216	0,89087	-1,7415
24,35	4,16		0,266	1,09709	-2,156
24,44	3,356		0,316	1,30331	-2,558
24,4	2,544		0,366	1,50953	-2,964

Figure 39: Data from calibration of thrust and torque scales

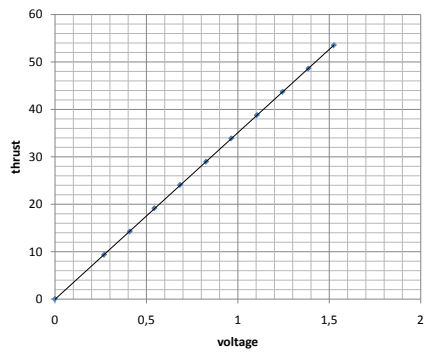
## A.2 Calibration curves



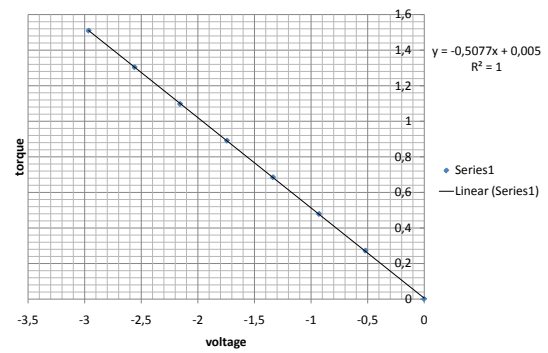
(a) Pitot tube



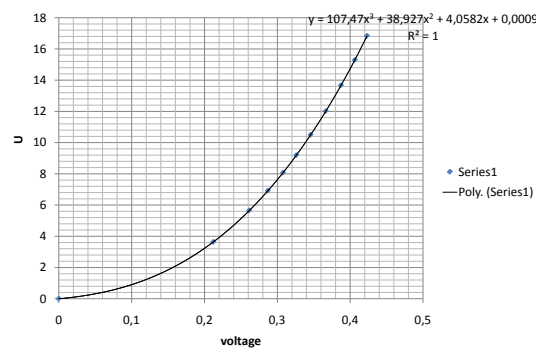
(b) Contraction wind speed



(c) Thrust



(d) Torque



(e) Hot wire

Figure 40: Calibration curves

# B Reference speed

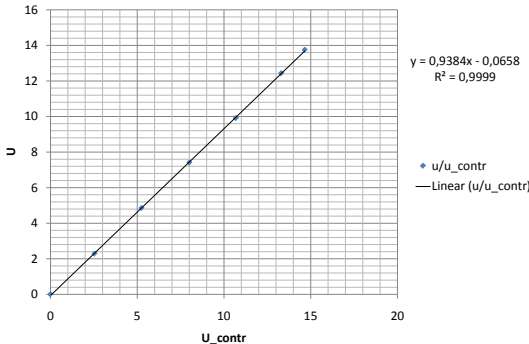


Figure 41: Ratio of speed at hub height vs speed measured at the contraction



# C Experimental data

## C.1 Wake measurements

Huge amount of data were gathered during the experimental work for this paper, an example of the data is showed in figure 42

Atm. Pres.		767,0		102258,3		R (J/KgK)		287,05	
TSR=3.0 x=3.5D z=-R									
Temp [C]	pit	pit pos	dp	rho	u	hw pos	turb% 2 (%)	from FORTRAN SCRIPT	
22,06	-8,612			0	1,206729	0			
23,48	-1,75	325	68,62	1,200952	10,68999	390	0,696		
23,46	-1,757	260	68,55	1,201033	10,68418	325	0,929		
23,48	-1,759	195	68,53	1,200952	10,68298	260	1,742		
23,45	-2,14	130	64,72	1,201074	10,38124	195	3,742		
23,49	-3,433	97,5	51,79	1,200912	9,287149	162,5	7,63		
23,49	-4,972	65	36,4	1,200912	7,785923	130	12,773		
23,49	-6,474	32,5	21,38	1,200912	5,9671	97,5	21,762		
23,5	-7,071	0	15,41	1,200871	5,066034	65	30,041		
23,52	-6,631	-32,5	19,81	1,20079	5,744122	32,5	36,037		
23,54	-5,176	-65	34,36	1,200709	7,565238	0	37,42		
23,58	-3,512	-97,5	51	1,200548	9,217442	-32,5	35,435		
23,58	-2,185	-130	64,27	1,200548	10,34736	-65	31,599		
23,62	-1,789	-162,5	68,23	1,200386	10,66209	-97,5	22,703		
23,65	-1,757	-195	68,55	1,200264	10,6876	-130	13,761		
23,67	-1,728	-227,5	68,84	1,200184	10,71055	-162,5	7,211		
23,68	-1,711	-260	69,01	1,200143	10,72394	-195	3,985		
23,75	-1,691	-325	69,21	1,19986	10,74074	-260	1,629		
23,79	-1,716	-390	68,96	1,199699	10,72204	-325	0,98001		

Figure 42: Exaple of data gathered in wake measurements

## C.2 Pressure measurements on cylinder surface

Pressure measurements on cylinder

p 751,5 mmHG  
100191,8 Pa

E0 -8,447

hole #	temp	rho	E	e	dyn pres	$\Delta p$	C_p
9,00	19,90	1,19	-1,82	1,10	66,45	0,00	1,00
10,00	20,50	1,19	-5,95	0,42	24,91	-24,91	0,63
11,00	20,30	1,19	0,53	1,50	90,09	-90,09	-0,36
12,00	20,50	1,19	5,25	2,28	137,50	-137,50	-1,07
13,00	20,10	1,19	4,30	2,12	127,96	-127,96	-0,93
14,00	20,60	1,19	3,77	2,04	122,64	-122,64	-0,85
15,00	19,80	1,19	3,81	2,04	122,99	-122,99	-0,85
16,00	20,60	1,19	4,63	2,18	131,23	-131,23	-0,97
1,00	20,40	1,19	4,90	2,22	133,96	-133,96	-1,02
2,00	20,40	1,19	4,63	2,18	131,28	-131,28	-0,98
3,00	20,40	1,19	4,24	2,12	127,39	-127,39	-0,92
4,00	20,40	1,19	4,08	2,09	125,69	-125,69	-0,89
5,00	20,40	1,19	4,20	2,11	126,94	-126,94	-0,91
6,00	20,50	1,19	5,38	2,30	138,80	-138,80	-1,09
7,00	20,40	1,19	0,77	1,54	92,46	-92,46	-0,39
8,00	20,50	1,19	-5,61	0,47	28,42	-28,42	0,57

Figure 43: Data from pressure measurements on cylinder surface

### C.3 $C_P$ and $C_T$

p_atm	748,50 mHg	99791,7 Pa								
R_spec	287,05 J/KgK									
g	9,82									
D_R	0,85 m									
A_R	0,57 m <sup>2</sup>									
<b>Torque coeff</b>	-0,51	0,01								
<b>Thrust coeff</b>	35,13	-0,04	Thrust E0	-7,87	G_thrust	6,00				
<b>u_contr</b>	91,53	-0,36	Torque E0	8,40	G_torque	2,00				
<b>U/U_contr</b>	0,94	-0,07	Contr E0	-7,19	G_contr	4,00				
rpm	w[rad/s]	TSR	Temp	rho	Torque	E_contr	Thrust	de_contr	dp_contr	
312,00	32,67	1,44	24,19	1,17	7,38	-4,44	-6,02	0,69	62,68	
416,00	43,56	1,92	24,33	1,17	7,16	-4,44	-5,89	0,69	62,68	
464,00	48,59	2,14	24,38	1,17	7,05	-4,44	-5,81	0,69	62,56	
532,00	55,71	2,45	24,40	1,17	6,85	-4,44	-5,70	0,69	62,63	
644,00	67,44	2,97	24,44	1,17	5,90	-4,44	-5,41	0,69	62,59	
708,00	74,14	3,26	24,48	1,17	5,62	-4,44	-5,23	0,69	62,59	
788,00	82,52	3,63	24,49	1,17	4,57	-4,46	-4,88	0,68	62,24	
868,00	90,90	4,00	24,53	1,17	4,84	-4,46	-4,79	0,68	62,22	
928,00	97,18	4,28	24,53	1,17	5,07	-4,45	-4,75	0,69	62,34	
984,00	103,04	4,54	24,55	1,17	5,36	-4,46	-4,74	0,68	62,06	
1036,00	108,49	4,78	24,58	1,17	5,58	-4,46	-4,72	0,68	62,24	
1096,00	114,77	5,05	24,58	1,17	5,89	-4,45	-4,72	0,68	62,29	
1168,00	122,31	5,39	24,63	1,17	6,27	-4,46	-4,76	0,68	62,18	
1260,00	131,95	5,81	24,67	1,17	6,73	-4,46	-4,81	0,68	62,22	
1352,00	141,58	6,23	24,71	1,17	7,23	-4,45	-4,88	0,69	62,43	
1436,00	150,38	6,62	24,73	1,17	7,72	-4,46	-5,00	0,68	62,27	
1524,00	159,59	7,03	24,74	1,17	8,22	-4,44	-5,12	0,69	62,54	
1596,00	167,13	7,36	24,75	1,17	8,63	-4,44	-5,24	0,69	62,54	
1688,00	176,77	7,78	24,80	1,17	9,18	-4,45	-5,41	0,69	62,38	
Torque[Nm]	Thrust[N]	U_contr[m/s]	P_rot	P_wind	Drag[N]	C_P		C_T		
0,26	10,81	9,65	8,62	298,27	30,90	0,03	0,35			
0,32	11,58	9,65	13,89	298,34	30,90	0,05	0,37			
0,35	12,02	9,65	16,91	297,54	30,85	0,06	0,39			
0,40	12,64	9,65	22,16	298,05	30,88	0,07	0,41			
0,64	14,35	9,65	43,14	297,74	30,86	0,14	0,47			
0,71	15,42	9,65	52,62	297,76	30,86	0,18	0,50			
0,98	17,46	9,62	80,73	295,30	30,69	0,27	0,57			
0,91	17,98	9,62	82,67	295,16	30,68	0,28	0,59			
0,85	18,23	9,63	82,61	295,98	30,73	0,28	0,59			
0,78	18,32	9,61	80,06	294,02	30,60	0,27	0,60			
0,72	18,42	9,62	78,23	295,35	30,69	0,26	0,60			
0,64	18,41	9,63	73,79	295,67	30,71	0,25	0,60			
0,54	18,19	9,62	66,62	294,88	30,65	0,23	0,59			
0,43	17,86	9,62	56,60	295,23	30,68	0,19	0,58			
0,30	17,46	9,64	42,61	296,72	30,78	0,14	0,57			
0,18	16,75	9,63	26,67	295,59	30,70	0,09	0,55			
0,05	16,05	9,65	8,05	297,56	30,84	0,03	0,52			
-0,05	15,38	9,65	-8,80	297,57	30,84	-0,03	0,50			
-0,19	14,34	9,64	-34,12	296,44	30,76	-0,12	0,47			

Figure 44: Data from  $C_P$  and  $C_T$  experiments

## C.4 TI plots from $x=1.5D$

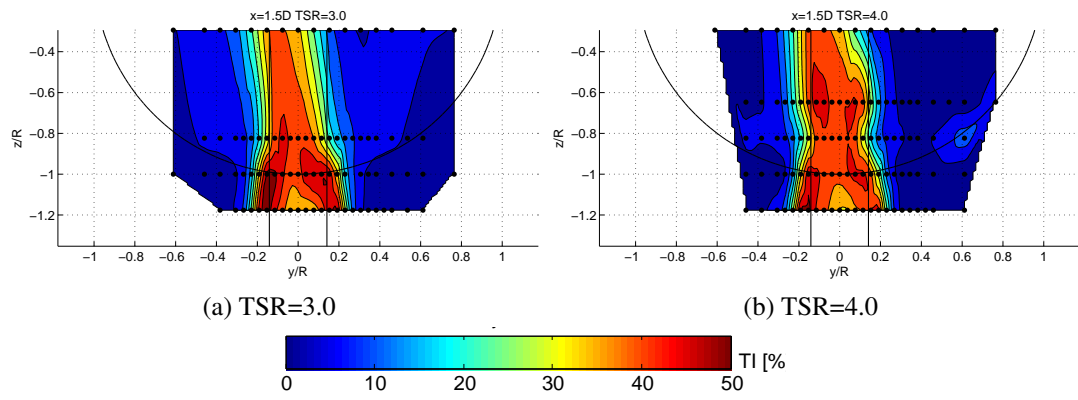


Figure 45: Contour plots of streamwise TI from  $x=1.5D$  for  $TSR=3.0$  and  $TSR=4.0$